National Renewable Energy Laboratory
A national laboratory of the U.S. Department of Energy
Office of Energy Efficiency & Renewable Energy
Innovation for Our Energy Future

Low-Cost Manufacturing of High-Efficiency, High-Reliability String Ribbon Si PV Modules

Final Subcontract Report
24 June 2005 – 31 October 2008

L. Felton
Evergreen Solar, Inc.
Marlboro, Massachusetts

Subcontract Report
NREL/SR-520-45902
May 2009

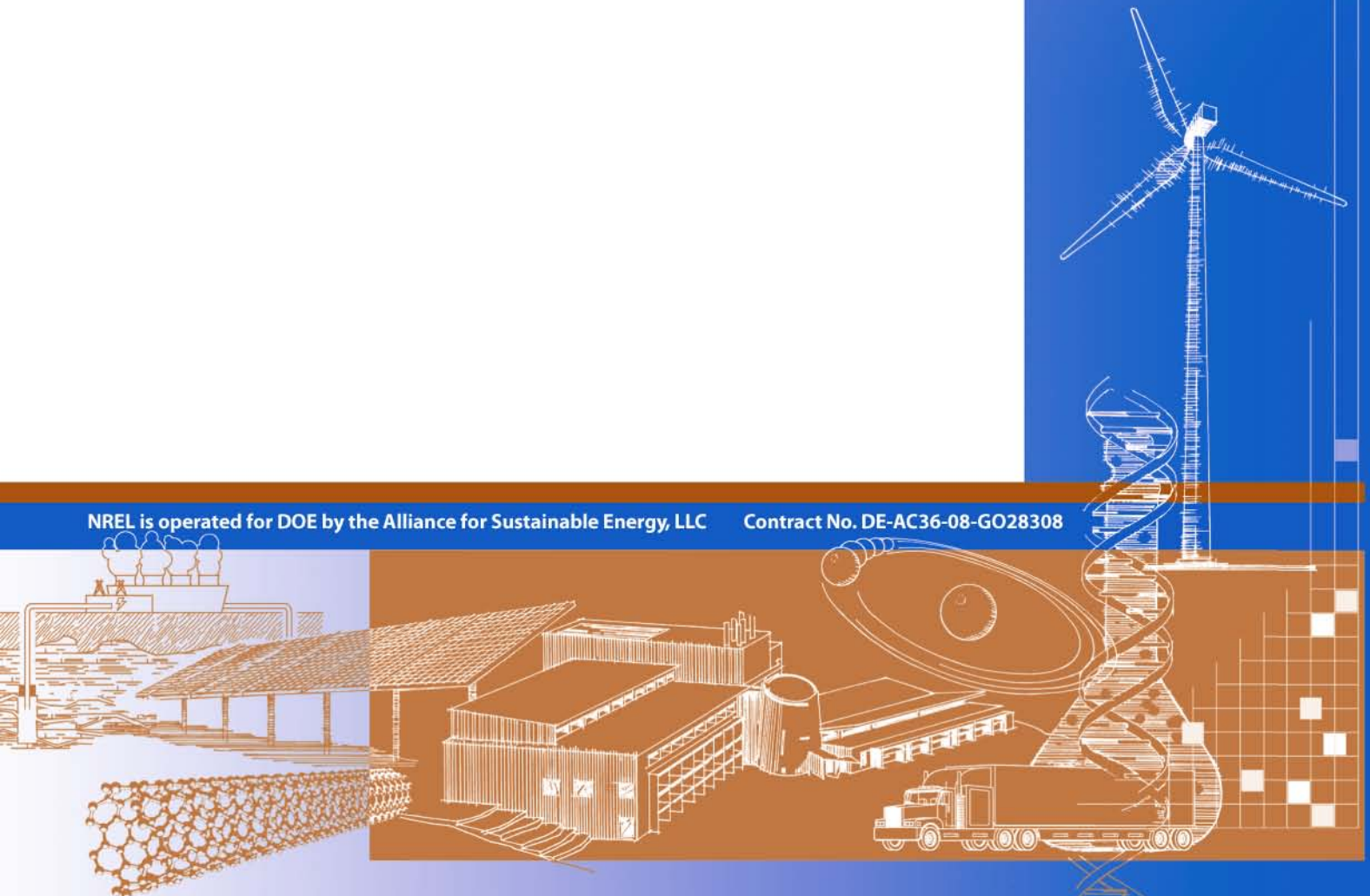

NREL is operated for DOE by the Alliance for Sustainable Energy, LLC Contract No. DE-AC36-08-GO28308

Low-Cost Manufacturing of High-Efficiency, High-Reliability String Ribbon Si PV Modules

Final Subcontract Report
24 June 2005 – 31 October 2008

L. Felton
Evergreen Solar, Inc.
Marlboro, Massachusetts

NREL Technical Monitor: R. L. Mitchell

Prepared under Subcontract No. ZAX-5-33628-08

Subcontract Report
NREL/SR-520-45902
May 2009

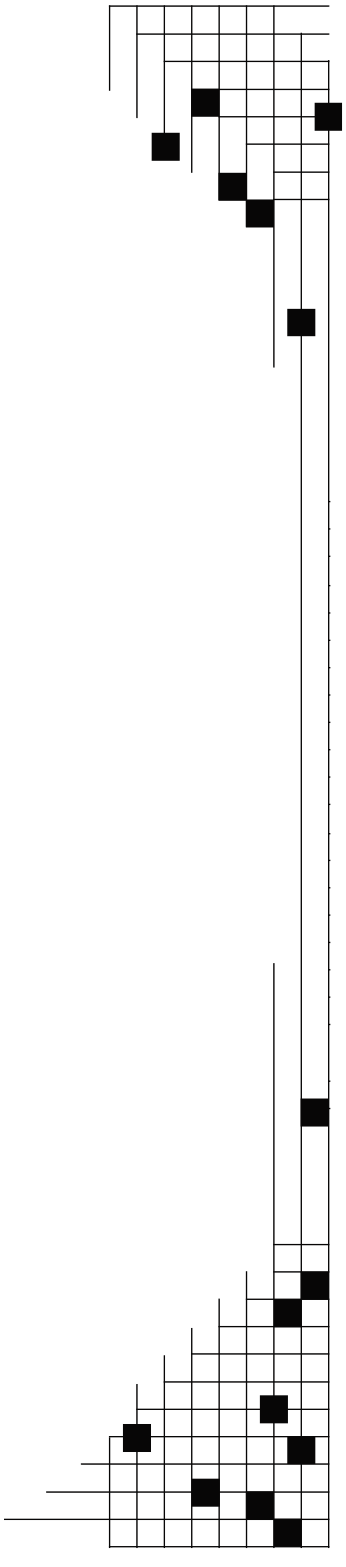

National Renewable Energy Laboratory
1617 Cole Boulevard, Golden, Colorado 80401-3393
303-275-3000 • www.nrel.gov

NREL is a national laboratory of the U.S. Department of Energy
Office of Energy Efficiency and Renewable Energy
Operated by the Alliance for Sustainable Energy, LLC

Contract No. DE-AC36-08-GO28308

Contents

Figures

Executive Summary

This report is presented to define the overall improvement process for 2008 in:

- Adaptive Thermal Processing – to improve string ribbon solar cell efficiency
- Cut-on-the-Fly (COTF) – to improve the cut-on the-fly manufacturing process
- Lamination – to improve process efficiency

For coherency sake, events are kept in the order of initial development.

For 2009 our improvement goals include:

- Adaptive Thermal Processing – TBD
- COTF – TBD
- Lamination - TBD

Section 1- Adaptive Thermal Processing

This section describes a chronology of events during the year with regard to adaptive thermal processing (Task 3.12). The progress of these tasks is presented as they occurred over the year. For each month there is a *Next Steps* description at the section end that outlines the expectations going forward.

January

1. Efficiency improvement of string ribbon silicon solar cells using Non-Contact Printing

One potential opportunity for higher cell efficiency is to improve finger print quality over screen-print quality by means of non-contact printing (NCP). An even more significant benefit with NCP should be cell yield, especially as the cell thickness is decreased from our current thickness of 190 microns to 150 microns and less. In addition to going to thinner cells, future String Ribbon cell efficiency improvements will target better surface passivation to reduce surface recombination velocity. And, of course, with lower surface recombination a thinner cell is also a more efficient cell. NCP enables higher cell efficiency through better print quality and by enabling higher yielding thin cell processing.

1.1 Background

Screen-printing on String Ribbon (SR) cells presents two problems that are significantly less of an issue with cast mc-Si wafers. These are wafer flatness and residual stress. String Ribbon cells are not as flat, including both macroscopic bow or warp as well as more microscopic undulation, and they have inherently more residual stress, due to the rapid rate that the wafers are drawn from the crystal growth furnace. These two SR-unique issues mean poorer metallization print quality and more screen-printing breakage than seen with cast wafers. We have sought to address both of these issues by employing non-contact printing (NCP) of the metallization. Possible NCP methods include ink-jet printing, direct-write of traditional screen-print paste, and aerosol spray, among others. Evergreen Solar has briefly explored ink-jet printing of Ag conductor, and more extensively studied direct-write and aerosol spray. Aerosol spray of Ag, developed by Optomec (Albuquerque, NM), has been employed primarily as a seed layer for light-induced plating (LIP) of a much thicker Ag layer. Unlike ink-jet and aerosol spray, direct write of Ag screen-print pastes, as developed by nScrypt (Orlando, FL), proposes to print metallization with width and height more similar to screen-printing.

nScrypt technology utilizes their unique combination of a valved tip, print tip design and ink pump to deliver a drop-on-demand, non-contact paste dispensing technology. The basic printing process for a 2BB design looks something like Figure 1.

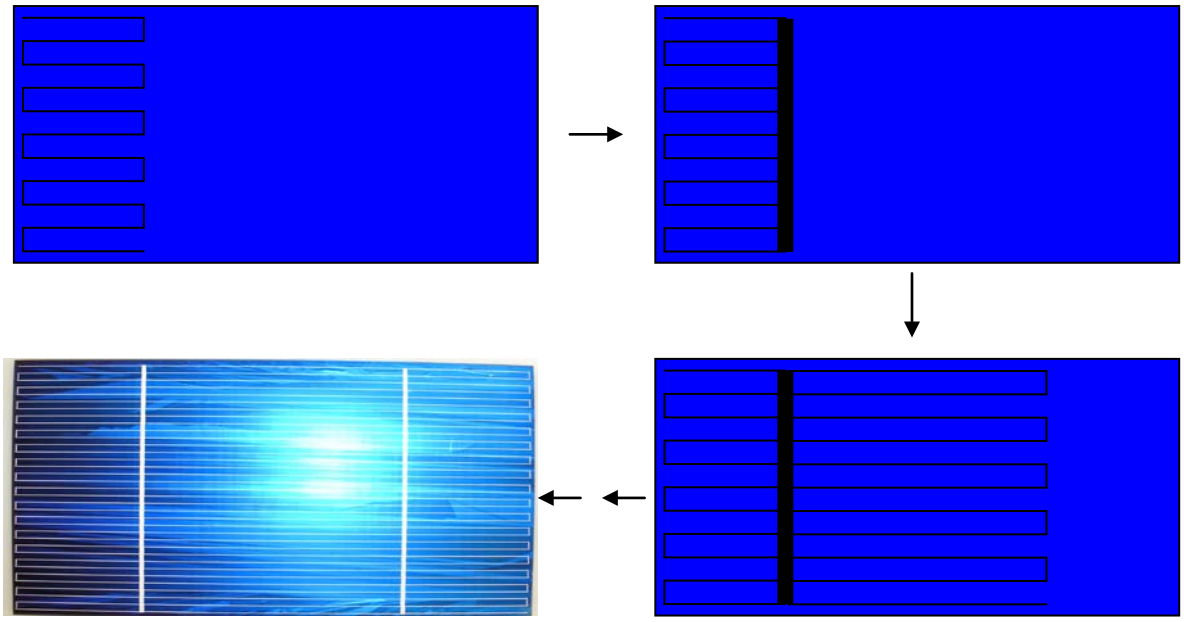

Figure 1. nScrypt's Non-contact Printing of a 2BB Pattern on Evergreen String Ribbon cell.

2. Solar Cell Processing

2.1 Cell Process Overview

Cell processing research discussed here uses production line GII String Ribbon wafers with an average wafer thickness of 190 µm and a p-type bulk resistivity averaging 3 Ω-cm. Solar cell processing begins with a dilute HF etch to remove a thin as-grown oxide. Wafers were textured in an inline process tool using chemistry described previously. Emitter formation by phosphorus diffusion employed a liquid $POCl_3$ source in a horizontal tube furnace, with process time and temperatures to achieve a mean sheet resistivity of either 75 or 90 Ω/□. A single-layer antireflective (SLAR) SiN_x coating was deposited by PECVD, followed by screen printing back Al and drying. The SOP cell groups employed a screen-printed Ag paste (Ferro 33-503) design of two busbars (2BB) with 35 fingers having 120 µm wide artwork. Metallization was completed by co-firing in a belt furnace. Front surface laser junction isolation completes cell processing.

NCP cells were printed with Al and dried and shipped to nScrypt for printing of the front metal. Cells were then co-fired and laser junction isolated upon return to Evergreen Solar.

2.2 Results and Discussion

Early cell test and finger characterization results using nScrypt printing with two commercial pastes are shown in Table 1.

Table 1. Cell Results and Characterization of nScrypt Printed SR Cells

Paste	# cells	Eff. (%)	Voc (V)	Isc (A)	FF (%)	Rs (mohms)	Rsh (mohms)	Rbb (mohms)	Finger WxH (µm)	Ag resistivity (ohm-m)
Ferro 503	7	15.13	0.595	4.043	75.08	7.1	50.9	19	148x29	2.7e-08
PV 149	8	15.16	0.595	4.061	75.13	8.3	63.8	26	155x31	4.1 e-08

As an initial effort, these results are strikingly good. There was no optimization of print tip or method to get these results. The print tip used was selected based on particle size (see below). Cell performance for this material is low, however. The screen-printed 2BB 35 x 120 cells using this material gave 15.54%, 0.604V, 4.093A, 75.49%FF, 8.9 mohm Rs, 61 mohm Rbb. Final finger width was about 119 microns. We noted that the lower Isc of the nScrypt cells is due to more shading because the line width that could be printed is limited by the particle size of the pastes, which is roughly 11-15 microns. nScrypt has demonstrated an approximate empirical relationship of 10-times the particle size for printed features. Hence, with particles as large as 15 microns, which limits the tip ID to about 17 microns to prevent clogging, the printed finger width is about 170 microns, which is roughly what was observed. The fingers typically shrink a little with firing. nScrypt cells were fired at 875ºC and lower FF could be several factors, including too much handling/poor handling at vendor or wrong firing temperature. The reason for the lower Voc is unclear.

The Ag finger resistivity is unusually low for the materials printed with nScrypt's process. Resistivity of screen-printed Ag fingers are more typically around 6.5 $x10^{-8}$ ohm-m for PV149 and 4.5 x 10^{-8} ohm-m for Ferro 33-503. Just for reference, bulk Ag is 1.7 $x10^{-8}$ ohm-m. Although the finger cross-sections are larger for the nScrypt fingers, it is likely that it is the consistent finger dimensions that lead to the lower resistivity. This is exactly one of the benefits that we would expect for the NCP process that lays down a uniform cross-section of conductor along the undulating SR surface, quite unlike what is observed when screen-printing the same pastes.

We also note that the nScrypt print quality is very impressive (see photos, Figure 2).

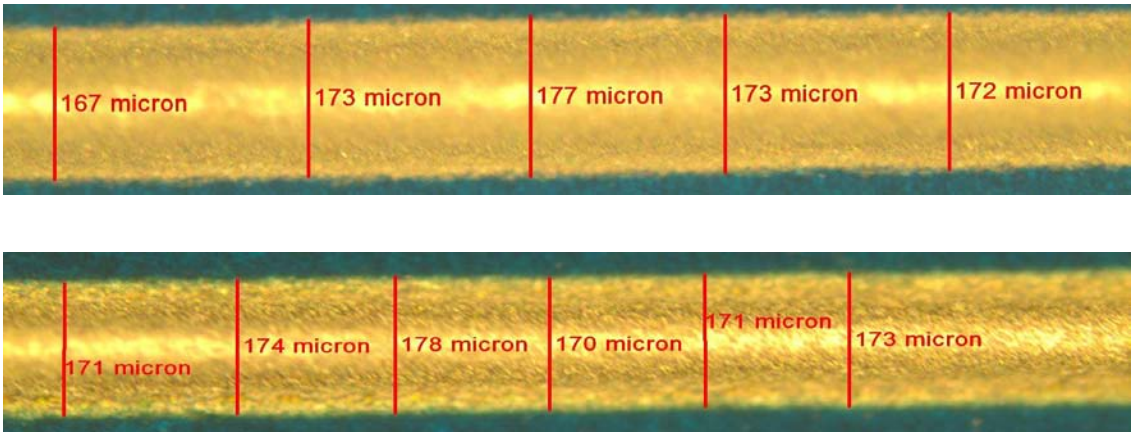

Figure 2. nScrypt Finger Images for PV149.

Note that finger widths reported in Table 1 are from profilometer and are considered more accurate.

Just to reiterate, print performance of commercial pastes is not a focus with this project, just an attempt to gather print data, print tool capability and develop a specification for nScrypt printable inks.

3. Next Steps

Next steps with nScrypt printing include obtaining smaller particle size pastes from DuPont and Ferro to achieve narrower line printing, followed by printing a multiple busbar pattern.

February

1 Efficiency improvement of string ribbon silicon solar cells using Optimized Metallization Firing

Traditional solar cell processing relies on co-firing of the back Al and front Ag to complete metallization of the cell. During this step a number of key processes take place: 1) the Al reacts with the silicon to form a eutectic layer, an Al-doped p^+ layer (back-surface field, or BSF), and a thin Al-diffused layer, 2) the Ag/frit paste fires through the densifying silicon nitride film to react with the emitter to form an ohmic contact to the heavily doped surface, and 3) hydrogen diffuses from the silicon nitride $Si_xN_yH_z$ layer, as well as near surface layer, into the bulk of the wafer where it is trapped at defect sites and passivates these defects. We investigated separating the bulk passivation/BSF formation and the front Ag contact formation using a double-fire recipe, with the goal of optimizing these individual steps. Here we report on initial developments with this new processing method.

1.1 Background

Firing studies have shown that in the co-fire process, typically V_{OC} improves with higher temperature, while FF decreases. This leads to a 'compromise' in the maximum cell efficiency. A typical firing study is shown in Figure 3.

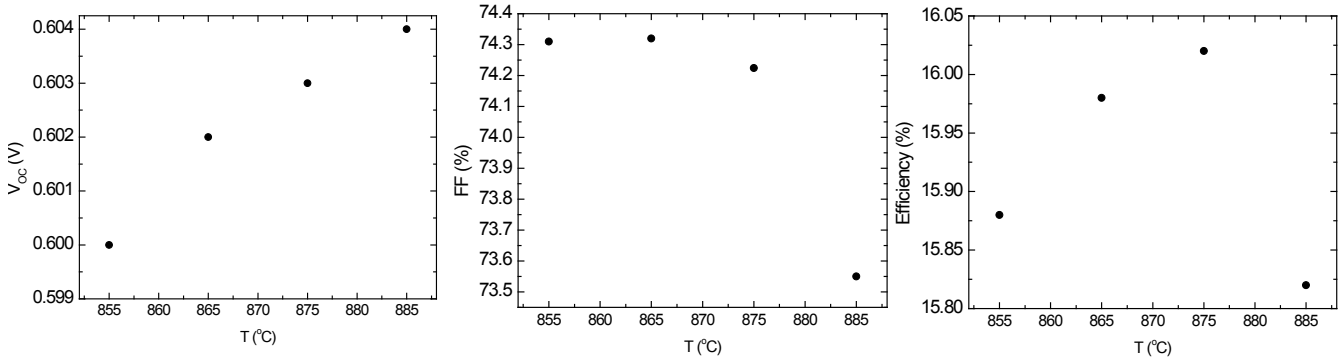

Figure 3. V_{OC}, FF and cell efficiency versus T typical for co-fire process.

Data illustrated are for multiple busbar cell process on String Ribbon.
The improvement in V_{OC} with increasing temperature is associated with the thickness and doping in the p^+ layer, leading to an improved BSF. The decrease in FF (increase in R_S, data not shown) is due to over firing of the front Ag, associated with firing deeper into the emitter and growth of a glass layer at the Ag finger-emitter interface. The behavior of I_{SC} is more variable, and has to do with the competing factors of hydrogen passivation and BSF formation. Double-fire, or sequential fire tries to separately optimize front metal contact formation and back contact formation/passivation step.

2 Solar cell Processing

2.1 Cell Process Overview

Cell processing research discussed here uses production line GII String Ribbon wafers with an average wafer thickness of 190 μm and a p-type bulk resistivity averaging 3 Ω-cm. Solar cell processing begins with a dilute HF etch to remove a thin as-grown oxide. Emitter formation by phosphorus diffusion employed a liquid $POCl_3$ source in a horizontal tube furnace, with process time and temperatures to achieve a mean sheet resistivity of either 75 Ω/□. A single-layer antireflective (SLAR) SiN_x coating was deposited by PECVD, followed by screen printing back Al and drying. The cell groups employed a screen-printed Ag paste (DuPont PV149) design of two busbars (2BB) with 35 fingers having 120 μm wide artwork. Metallization was completed by either co-firing or double-firing in a belt furnace. Double-fire process, also referred to as sequential fire, involves printing of the back contact Al and firing, followed by printing of the front Ag grid and firing. Front surface laser junction isolation completes cell processing.
In the experiment reported here (GII LOT # 33326TR), the double-fire design utilized the firing conditions in Table 2.

Table 2. Double-fire design.

	Group I			Group II			Group III			Group IV		
First fire (backs)	**850**	**850**	**850**	**870**	**870**	**870**	**890**	**890**	**890**	**910**	**910**	**910**
Second fire (fronts)	**840**	**855**	**870**	**840**	**855**	**870**	**840**	**855**	**870**	**840**	**855**	**870**

The control group is our SOP co-fire process that uses CT at about 875 ± 10 °C optimization groups

2.2 Results and Discussion

- **Co-fire: 15.41%, 0.603V, 4.097A, 74.74% FF**
- **Best double-fire: 15.65%, 0.608V, 4.113A, 75.11% FF**
- **All data**

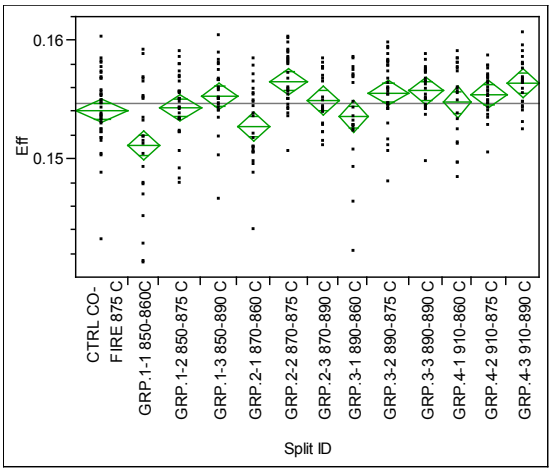

Level	Number	Mean
CTRL CO-FIRE 875 C	39	0.154052
GRP.1-1 850-860C	23	0.151162
GRP.1-2 850-875 C	31	0.154280
GRP.1-3 850-890 C	27	0.155278
GRP.2-1 870-860 C	24	0.152733
GRP.2-2 870-875 C	28	0.156525
GRP.2-3 870-890 C	23	0.154900
GRP.3-1 890-860 C	21	0.153561
GRP.3-2 890-875 C	31	0.155571
GRP.3-3 890-890 C	25	0.155718
GRP.4-1 910-860 C	21	0.154784
GRP.4-2 910-875 C	26	0.155409
GRP.4-3 910-890 C	24	0.156327

Figure 4. Double-fire cell efficiency groups plotted and tabulated.

All cell data were analyzed using a generalized linear model that analyzed individual firing conditions as well as interactions. A response surface plot for cell efficiency is shown in Figure 5.

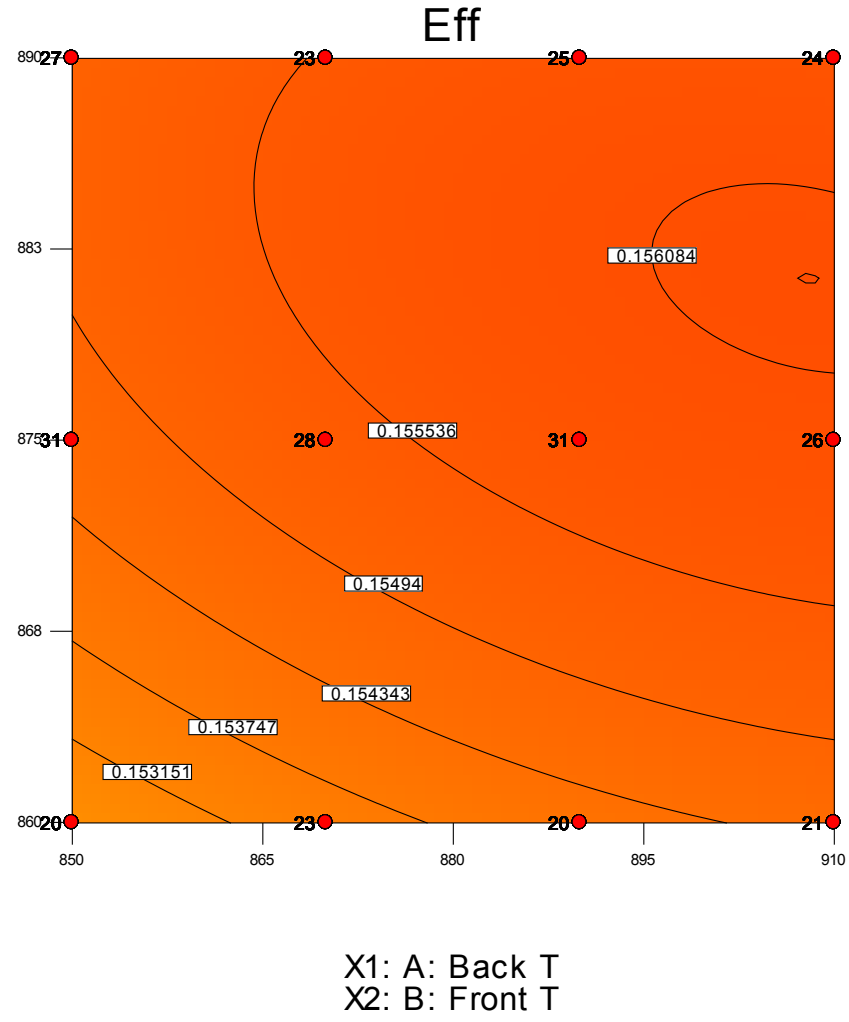

Figure 5. Response surface plot of double-fire experiment.

Based on this analysis the best double-fire process uses roughly 908 C for back Al firing, followed by about 882 C for front contact firing.

3. Next Steps

The data model shows definitively that the double-fire cell parameters Efficiency, Voc and FF are statistically better than the SOP co-fire. It is interesting that the best double-fire was 870ºC for back and 875ºC for front. This is a higher temperature for the front than expected and is the same as co-fire temperature. It is noteworthy, however, that an essentially equivalent cell efficiency was achieved for 910ºC back firing and 890ºC front firing. We believe that a secondary effect operative with the double-fire is the fact that the front contact is firing through densified SiN, as opposed to the co-fire situation, in which the silicon nitride is densifying during the front contact formation. The situation for hydrogen passivation in the double-fire deserves some comment. Although the I_{SC} data suggest that hydrogen passivation is not compromised in the double-fire process, independent determination of material upgrading using lifetime analysis of the finished cells is warranted.

Next steps: study new back Al pastes and repeat double-fire study with new Al and possibly new front Ag (Ferro 503 or Heraeus CL80-8978), as well as measure lifetime of double-fired cells.

March

1 Efficiency improvement of string ribbon silicon solar cells using Non-Contact Printing (Part II)

Previously we reported on non-contact printing (NCP) using nScrypt technology as a means of improving solar cell efficiency. Here we report on further developments with this method using refined Ag inks.

2 Solar cell Processing

2.1 Cell Process Overview

Cell processing research discussed here uses production line GII String Ribbon wafers with an average wafer thickness of 190 μm and a p-type bulk resistivity averaging 3 Ω-cm. Solar cell processing begins with a dilute HF etch to remove a thin as-grown oxide. Wafers were textured in an inline process tool using chemistry described previously. Emitter formation by phosphorus diffusion employed a liquid $POCl_3$ source in a horizontal tube furnace, with process time and temperatures to achieve a mean sheet resistivity of 75 Ω/□. A single-layer antireflective (SLAR) SiN_x coating was deposited by PECVD, followed by screen printing back Al and drying. The SOP cell groups employed a screen-printed Ag paste (Ferro 33-503) design of two busbars (2BB) with 35 fingers having 120 μm wide artwork. Metallization was completed by co-firing in a belt furnace. Front surface laser junction isolation completes cell processing.

NCP cells were printed with Al and dried and shipped to nScrypt for printing of the front metal. Cells were then co-fired and laser junction isolated upon return to Evergreen Solar.

2.2 Results and Discussion

Following the earlier printing with commercial DuPont pastes (PV147 and 149), DuPont developed two modified pastes containing somewhat different formulations as well as smaller particle size. The NCP project goal is to achieve a final fired finger width of about 60 microns. For nScrypt this means printing through a tip ID of about 40-50 microns, which requires a particle size of 4 microns or less. NB: There was an error in the Jan 2008 Monthly that stated the tip size for 15 micron particles needs to be 17 microns. It should have said that the tip ID has to be about 150 microns. Ideally the particles should be considerably

less than 4 microns, more like 1-2 microns, since clogging of the pen tip is a function of agglomeration of the paste, as well as a function of the particle size. It unclear at this time what paste specifications are required for printing a specific line width. What is known, roughly, is that the following set of factors determines line width:

1. Tip size: Based on empirical performance and limited modeling, ID must be ~10X particle size
2. Pressure
3. Paste rheology
4. Speed
5. Height of tip (2^{nd} order effect)

Armed with the most recent DuPont inks, nScrypt printed with a range of pen tips. The best results were obtained with an 80 micron ID tip with PV147 MOD II. This batch of ink shows great improvement over the last ink (PV147 MOD I). It flows through a 50 micron ID tip for awhile and an 80 micron tip indefinitely. This is in contrast to PV147 MOD I, which can flow readily through a 100 micron tip and eventually clogs an 80 micron tip. PV147 MOD II can also flow through 25 micron tip for a limited time, while PV147 MOD I clogged this tip immediately. Unfortunately, PV147 MOD II is not as thick as PV147 MOD I, so it tends to spread on the cell and make the line wider. The majority of the fingers are in the range of 75-80 microns wide. If the viscosity of the ink is more similar to PV147 MOD I it is likely nScrypt could print finer lines, of the order of 60 microns. This would be very significant since it addresses a key objective of the NCP program, which is writing lines of the order of 60 microns.

Cell results for the three DuPont pastes are shown in Table 3.

Table 3. Cell results and characterization of nScrypt printed SR cells, along with the screen-printed control group.

Paste	Cell Qty.	Efficiency (%)	Voc (V)	Isc (A)	FF (%)	Rs (mohm)	Rsh (mohm)	Rbb (mohm)	WxH µm	Ag Resistivity (ohm-m)
Screen print Ferro 33-503	25	15.54	0.604	4.093	75.49	8.9	68.3	48	116x23.5	4.32
DuPont PV149	8	15.16	0.595	4.061	75.13	8.3	63.8	26	155x31	4.1e-08
PV147 MOD I	6	15.34	0.600	4.176	73.46	12	95.6	86	103x24	7.1e-08
PV147 MOD II	6	15.73	0.603	4.165	74.39	10.8	99.0	100.7	96x15	4.6e-08

The screen-printed 2BB 35 x 120 cells (Ferro 33-503) using this String Ribbon material gave 15.54% (Table I), with a final finger width of about 116 microns. We used Ferro 33-503 as the screen-print 'standard' since this ink performs somewhat better than PV149. We noted that the lower Isc of the PV149 nScrypt cells is due to more shading because the line width that could be printed is limited by the particle size of the paste, which is roughly 11-15 microns. nScrypt cells were fired at 875ºC and the lower FF, despite lower Rs, is unclear, as is the much lower Voc. Most likely the nScrypt PV149 cells have lower contact resistance. The improvement with PV147 MOD I is associated with higher Isc (lower shadow

loss), though the Isc is considerably larger than predicted by shadow loss. The lower FF, higher Rs, of MOD I is due in part to poorer conductivity. Additional contributing factors could include too much handling/poor handling at vendor or wrong firing temperature, leading to high contact resistance. The reason for the lower Voc for both PV149 and PV147 MOD I is unclear.

The significant improvement with PV147 MOD II, with a boost of about 0.2% absolute over the screen-printed group, is associated with narrower fingers, leading to higher currents, and better conductivity, leading to okay FF. The overall higher Rs suggests that more fingers are needed. The boost in Isc is somewhat larger than expected, based on the increase in active area; however, the shadow loss calculation is based on a limited sampling of finger widths.

3. Next Steps: Non-Contact Printing of multiple busbar cells

Printing progress with NCP has been significant, due in large part to smaller particle inks. While printing a 2BB pattern is a convenient test structure to gauge progress with NCP on String Ribbon cells, our future cell technology will employ a multiple busbar design similar to those described previously. Our next objective with NCP is to print multiple busbar cells, and results of these efforts will be reported in the coming months.

April

1. Efficiency improvement of string ribbon silicon solar cells with a passivated back surface cell

A new String Ribbon efficiency improvement program, based on a passivated back surface (PBS) cell design, was initiated in March. Here we summarize program objectives, research plan and some initial results.

1.1 Background

The present state-of-the-art rear surface structure of industrial silicon solar cells is a screen-printed and thermally fired Al back surface field (Al-BSF). The Al-BSF plays a crucial role in the electrical performance of the solar cell by substantially reducing the recombination of minority carriers at the surface, increasing I_{SC} and V_{OC}. The recombination rate of carriers at the surfaces is characterized by the surface recombination velocity (SRV), which can be determined indirectly from minority carrier lifetime using the right experimental conditions. A typical value of the Al-BSF SRV is around 700 cm/s. We have modeled the back SRV of our cells at around 800 cm/s. Additional modeling that examined further reduction in the recombination at the back surface suggests that better passivation of this surface could lead to a substantial improvement in cell efficiency, as shown in Figure 6.

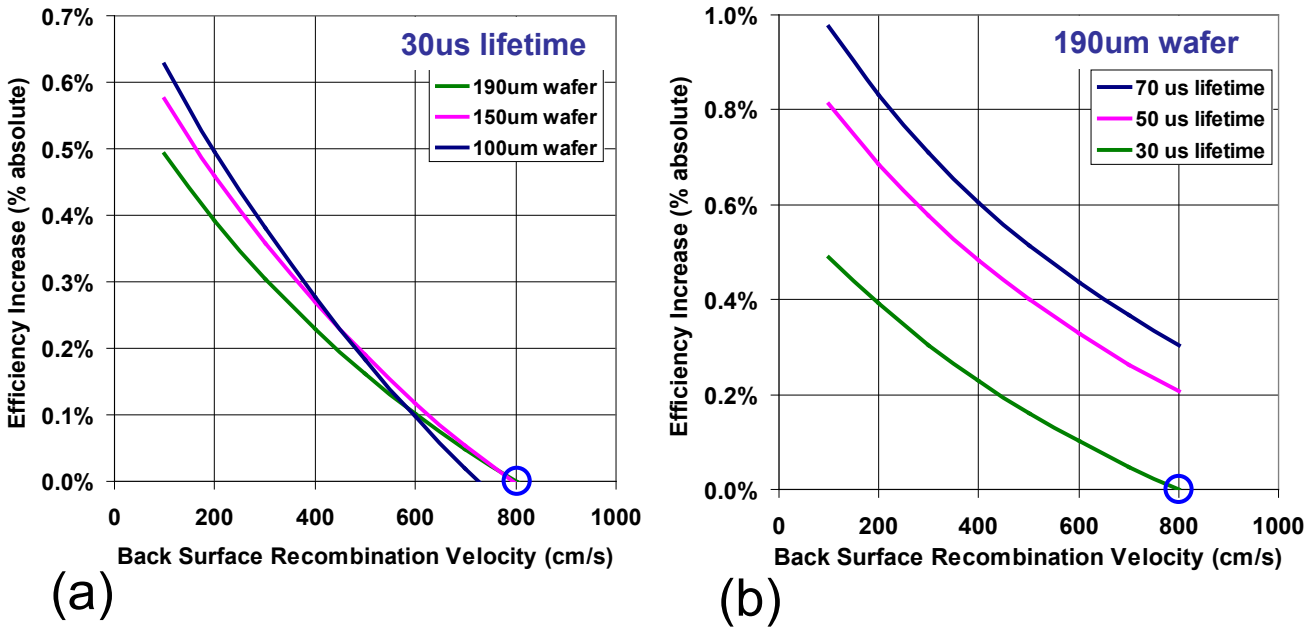

Figure 6. Cell efficiency improvement versus back surface recombination velocity for Evergreen's String Ribbon cells based on PC-1D modeling.

The current cell Al-BSF recombination velocity is estimated at about 800 cm/s. Modeling assumed an average 30 µs lifetime, typical of our SOP cell process. The model also considered the impact of reducing cell thickness from our present value of 190 microns (a) as well as reducing the cell thickness (b). The inescapable conclusion of Figure 1 is that the Al-BSF is a significant limitation of String Ribbon solar cell efficiency, especially for thinner cells with longer lifetime. An efficiency improvement of 0.3% absolute is postulated for the current String Ribbon wafer, typically 190 microns thick and about 30 microsecond lifetime, using better back surface passivation with a realistic SRV of 300 cm/s for the metallized surface. However, with efforts to reduce String Ribbon wafer thickness to 150 microns, a goal proposed for 2010, a PBS cell with 30 microsecond lifetime could achieve an efficiency boost of about 0.45%.

The principal features of a PBS cell include the passivation of the back surface along with the metallization scheme to make contact through this passivation layer. The best known surface passivation layer is a thermal oxide,[1, 2] though other layers have been investigated.[3] While SRV values as low as 30-50 cm/s have been documented for carefully cleaned and oxidized sc-Si wafers, addition of metal contacts to this layer significantly increases the SRV to about 300 cm/s in the best circumstances. The final SRV for the PBS cell depends on the aggregate cell processing, including the type of passivation layer, the cleaning and handling both prior and subsequent to formation of the passivating layer, and the amount of metal coverage.

While there has been extensive reporting of PBS cell structures and results for sc-Si and high quality/lifetime cast mc-Si, much less is known about the surface passivation of 'more typical' mc-Si, including String Ribbon. In the following section we outline our plan for investigation of surface passivation of String Ribbon wafers and the design of a PBS String Ribbon cell.

2. Passivated Back Surface Cell Processing

2.1 PBS Cell Process Overview

Our proposal for a PBS String Ribbon cell (Node 10) can best be understood by comparison with our current higher efficiency cell (Node 8), as shown in the scheme in Figure 7.

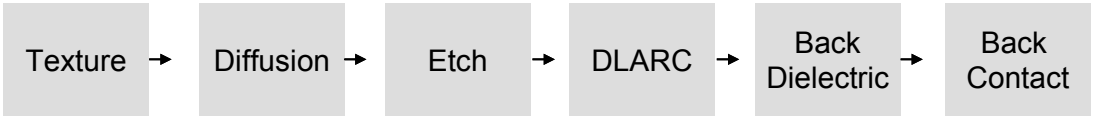

Node 8	Double-sided	POCl double-sided	2% HF glass etch	Sputtered	None	DSP Ag + DSP Al for back surface field (BSF)
Node 10	**Single-sided w/ hydrophilic treatment**	POCl or **inline single-sided**	**Possible back-side Si etch + GE with added clean**	**CVD**	**CVD**	• **DSP Al fire-through or** • **Laser ablation + spray Al or** • **Chemical etch + spray Al**

Figure 7. Cell Process Overview

The Node 8 cells have been described frequently in these reports. The cell process uses production line GII String Ribbon wafers with an average wafer thickness of 190 µm and a p-type bulk resistivity averaging 3 Ω-cm. Solar cell processing begins with a dilute HF etch to remove a thin as-grown oxide. Wafers are textured in an inline process tool using chemistry described previously to produce a double-sided texture. Emitter formation by phosphorus diffusion employs a liquid $POCl_3$ source in a horizontal tube furnace, with process time and temperatures to achieve a mean sheet resistivity of 75 Ω/□, with an emitter around the entire wafer. A single-layer antireflective (SLAR) SiN_x coating is deposited by PECVD, followed by screen printing back Al and drying. The SOP cell groups employed a screen-printed Ag paste (Ferro 33-503) design of two busbars (2BB) with 35 fingers having 120 µm wide artwork. Metallization is completed by co-firing in a belt furnace. Front surface laser junction isolation completes cell processing.

In contrast, our proposed PBS cell design requires single-sided texture on the front only, to improve the back surface passivation, a single-side emitter, also on the front only, and an optimized back surface that simultaneously minimizes SRV and series resistance.

3. Next Steps: PBS back contact designs and surface passivation layers

Over the coming months we will report on our results with passivating the surfaces with a variety of dielectric films as well as attempts to make electrical contact to the cell through these films while minimizing the metal contact surface area.

1. Schultz, O.; Glunz, S. W.; Goldschmidt, J. C.; Lautenschlager, H.; Leimenstoll, A.; Schneiderlöchner, E.; Willeke, G. P. In *Thermal oxidation processes for high efficiency multicrystalline silicon solar cells*, 19th European Photovoltaic Solar Energy Conference, Paris, 7-11 June, 2004; Paris, 2004.
2. Lemke, A.; Furtwängler, H.; Rentsch, J.; Biro, D.; Preu, R. In *Thermal oxidation and wet chemical cleaning of silicon wafers for industrial solar cell production*, 22nd European Photovoltaic Solar Energy Conference and Exhibition, Milan, Italy, 3-7 September, 2007; Milan, Italy, 2007.
3. Aberle, A. G., *Advanced surface passivation and analysis*. University of New South Wales: Sydney, 1999.

May

1 Efficiency improvement of string ribbon silicon solar cells using Non-Contact Printing (Part III)

Previously (Jan and Mar, 2008 Monthly Reports) we reported on non-contact printing (NCP) using nScrypt technology as a means of improving solar cell efficiency. Here we report on further developments with NCP collaborator Optomec to print our multiple busbar cell design. See Oct and Dec 2008 Monthly reports for previous discussion of multiple busbar cell design.

2 Solar cell Processing

2.1 Cell Process Overview

Cell processing research discussed here uses production line GII String Ribbon wafers with an average wafer thickness of 190 μm and a p-type bulk resistivity averaging 3 Ω-cm. Solar cell processing begins with a dilute HF etch to remove a thin as-grown oxide. Wafers were textured in an inline process tool using chemistry described previously. Emitter formation by phosphorus diffusion employed a liquid $POCl_3$ source in a horizontal tube furnace, with process time and temperatures to achieve a mean sheet resistivity of 75 Ω/□. A single-layer antireflective (SLAR) SiN_x coating was deposited by PECVD, followed by screen printing back Al and drying. The SOP cell groups employed a screen-printed Ag paste (Ferro 33-503) design of two busbars (2BB) with 35 fingers having 120 μm wide artwork. Metallization was completed by co-firing in a belt furnace. Front surface laser junction isolation completes cell processing. Cells were tested and then 1.5-mm wide tab material was soldered to the busbars for more similar comparison with the wired, multiple busbar cells, also referred to as multi-wire (MW) cells.
NCP cells were printed with Al and dried and shipped to Optomec for printing of the front fingers. Several groups of multiple busbar were completed at Optomec, and the experimental design included a 1:1 comparison of 2BB with Optomec MW cells on the same batch of wafers. Groups were either 6- or 10-pass Optomec fingers (40-count) with Ferro CK1590-1. Cells were returned to ES for screen-printing of the solder pads (Ferro 33-503), and fired. Saw JI was required, instead of our SOP laser JI, because fingers run off the ends. Wiring was performed using Polytabber #1.

2.2 Results and Discussion

Cell data are reported in Table 4 and cell efficiency results are also shown in Figure 8.

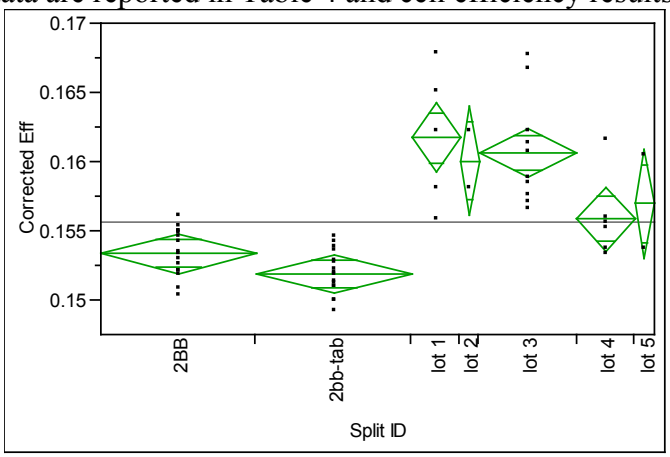

Figure 8. Efficiency versus lot ID for Optomec MW cells and the ES SOP 2BB controls.

Table 4. Cell parameters for 2BB and the five lots of Optomec multiple busbar cells.

Level	Number	Mean	Voc	Isc	FF	Rs
2BB	16	0.153338	0.602163	4.09668	74.5901	0.010451
2bb-tab	16	0.151866	0.600304	4.15563	73.0521	0.012606
lot 1	5	0.161700	0.604170	4.3425	73.9432	0.011951
lot 2	2	0.160049	0.602392	4.3362	73.5290	0.011959
lot 3	10	0.160642	0.604194	4.3706	72.9910	0.013181
lot 4	6	0.155820	0.602366	4.3465	71.4200	0.015885
lot 5	2	0.156958	0.601781	4.3188	72.4633	0.014783

Note that the Optomec cells are smaller (115.44 cm^2, versus 120 cm^2 2BB cells) due to saw JI so to compare efficiency the cell test area is corrected. To compare Isc boost I corrected tested Isc to what it would be for 120 cm^2 area, same as 2BB**.** Lot #1 (6-pass) had no problems at Optomec. Lot#4 is 10-pass and supposedly worked okay. Lot#2 (6-pass) had one nozzle (in 10) printing wide, but not a major flag. Lots#3 and 5 (both 6-pass) should have been identical to Lot#1. *Lack of consistency of groups is concerning.* Lots #2 and 5 had too few cells for meaningful conclusion. High Rs, especially at 10-pass fingers, highlights a concern with this print process. As stated above, the heights are very variable, as shown in a profile of a short section of a 6-pass finger in Figure 9.

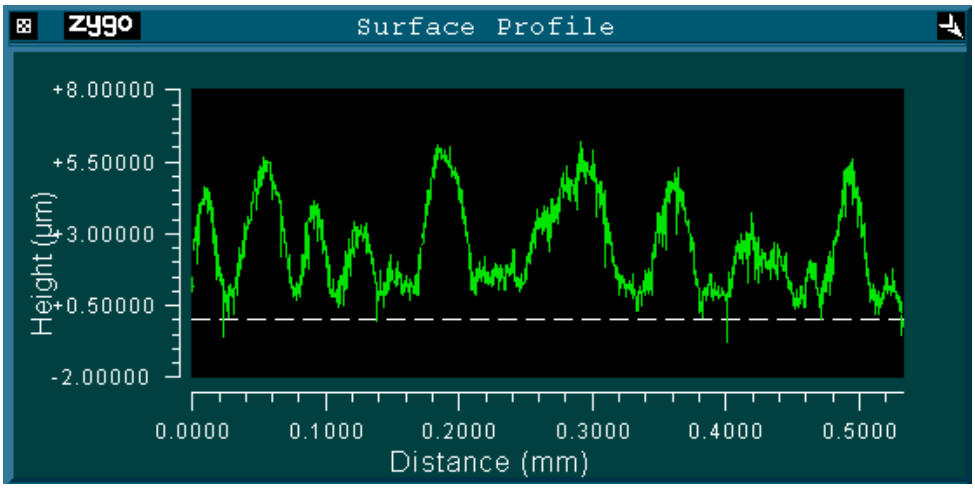

Figure 9. Zygo profile of Lot#1 finger (6-pass) along length of finger, cell #4.

Note the highly variable finger height, roughly 2.8 ± 2.8um. Typical finger height for one group of screen-printed MW cells was 13 um ± 3.4um and finger width 55± 8.7um using the profilometer.

We note remarkably good results for one group of Optomec cells (Lot #1), however, we also note that this is a very convoluted and variable cell process, due to current limitations of Optomec technology. Optomec is currently unable to print solder pads, though they could print solder lines, or bars, and fingers run off the end of the cells, requiring saw-JI. The Optomec MW cells would improve substantially (0.3%) with more fingers at fewer passes. Multiple passes produces much finger height variability.

The following analysis further summarizes the cell data reported here:

Tabbed 2BB vs. fixture 2BB: -0.14% absolute, which looks like it is roughly what the mean loss is when we tab the 2BB cells.
Tabbed 2BB: 15.19%, 0.600V, 4.156A, 73.04% FF, 12.6 mohm Rs
Best MW: 16.17%, 0.604V, 4.343A, 73.94% FF, 12.0 mohm Rs
MW vs. tabbed 2BB Δ : 0.98%, 4mV, 0.187A, 0.90%FF, -0.6 mohm Rs

Compare these numbers with our last screen-printed MW vs. tabbed 2BB experiment:
Tabbed 2BB: 15.20%, 0.601V, 4.124A, 73.53% FF, 12.4 mohm Rs
MW: 16.24%, 0.610V, 4.274A, 74.72% FF, 10.5 mohm Rs
MW vs. tabbed 2BB Δ : 1.04%, 9mV, 0.150A, 1.19%FF, -1.9 mohm Rs

3.0 Next Steps: Refinement of Optomec Non-Contact Printing of multiple busbar cells and nScrypt NCP of multiple busbar cells

Our next objective with NCP is to launch an nScrypt NCP multiple busbar cell program, as well as refine the Optomec process with more fingers at fewer passes and Optomec solder bars for wiring, rather than screen-printing of the solder pads.

June

1 Efficiency improvement of string ribbon silicon solar cells with a passivated back surface cell

The passivated back surface (PBS) cell program was introduced in the April Monthly Report, with initial results for several films reported in the May report. Here we describe further improvement of surface passivation using dielectric films passivated following plasma pre-clean, as well as results for an atomic layer deposition (ALD) alumina film.

1.1 Background

A standard means of determining the SRV (also S or S_{eff}) of a dielectric film is to measure the lifetime of a substrate coated with the film on both surfaces. The SRV can then be extracted using the specific solution for the PCD lifetime and SRV (developed previously, May 2008 Monthly report)

$$\frac{1}{\tau_{eff}} = \frac{1}{\tau_{bulk}} + \frac{2S_{eff}}{t}$$

Solving for SRV using this equation requires knowledge of τ_{bulk} as well as measurement of τ_{eff} of the passivated wafer. Initially, we used sc-Si as a model system to evaluate dielectric film surface passivation. This simplified several complications using String Ribbon wafers, which include 1) non-uniform thickness within the wafer, 2) aereal inhomogeneity of surface passivation for different grain orientations, 3) low as-grown lifetime of String Ribbon wafers, and 4) high variability of lifetime within the wafer. However, surface passivation of SR wafers is our objective, and so we have begun to introduce measurement of recombination velocity of passivating films on String Ribbon material, and these are reported here as well.

Our process begins with measurement of the bulk lifetime of sc-Si Cz and mc-SR wafers prior to film deposition using an organic surface passivation based on an iodine/methanol reaction. We then clean the wafers to remove the organic film and deposit the passivating film(s), followed by lifetime measurement of the effective lifetime of the wafers. SRV for the surface passivation layer can be determined using the above equation.

2 Passivating Surface Films

2.1 Results and discussion

We deposited or grew dielectric films on both sides of HF cleaned sc-Cz wafers and mc-SR wafers (2 wafers per film). Most of the film deposition was performed in our Roth and Rau (R&R) AK-800 RMW/RF-PECVD tool, however, we also deposited some Alumina (Al_2O_3) by either Evergreen PVD or Cambridge Nanotech atomic layer deposition (ALD), and New Jersey Institute of Technology (NJIT) grew some wet oxide. In addition, we performed more evaluation of dry etch pre-clean for additional pre-deposition processing to remove adventitious hydrocarbons and water. It should be noted that errors in SRV calculations for SR wafers may be large due to low bulk carrier lifetime of as-grown string ribbon wafers as well as variation due to grain orientation.

Table 5 and Table 6 report lifetime and SRV data for deposited films.

Table 5. Lifetime (µs) and SRV (cm/s) versus film type, pre-process and substrate for wet oxide films.

Split	As-Received Lifetime (us)	IM-Passivated Lifetime (us)	As-Processed Lifetime (us)	Post-Fire Lifetime (us)	SRV (cm/s)
NJIT RCA+WETOX on CZ	4.3	180.1	25.2	36.4	383.0
NJIT Pihranna+WETOX on CZ	4.4	197.3	27.4	32.3	453.5
NJIT RCA+WETOX on SR	1.1	2.7	1.9	2.2	1016.4
NJIT Pihranna+WETOX on SR	1.0	2.0	2.5	1.6	1506.4
SEMCO WETOX on SR	1.1	2.8	1.6	0.9	7300.0
SEMCO WETOX on CZ	4.2	180.9	3.8	4.1	4181.1

Table 6. Lifetime and SRV versus film type (ALD or PVD alumina) and substrate.

Wafer ID	Process Type	Thickness	As-Received Lifetime (us)	IM-Passivated Lifetime (us)	As-Deposited Lifetime (us)	As-Nitrided Lifetime (us)	Post-Fire Lifetime (us)	SRV (cm/s)
CZ-002	CZ-ALD-002	500	4.4	256.2	101.2	65.2	67.0	105
CZ-001	CZ-ALD-001	1000	4.6	245.9	95.3	73.5	79.1	113
CZ-007	CZ-PVD-007	500	4.4	261.2	9.6	57.0	63.9	1764
CZ-008	CZ-PVD-008	1000	4.6	234.4	4.6	41.0	57.2	3740
CZ-009	CZ-PVD-009	500	4.6	226.3	4.7	53.1	58.4	3619
CZ-010	CZ-PVD-010	1000	4.5	217.9	4.4	56.1	59.9	3878
SR-089	SR-ALD-089	1000	2.3	11.5	9.7	6.0	3.5	166
SR-100	SR-ALD-100	500	2.2	13.4	11.7	10.3	6.8	117
SR-008	SR-PVD-008	1000	2.3	8.6	1.3	8.2	7.2	7147
SR-009	SR-PVD-009	500	2.3	6.8	1.0	9.5	8.9	8549
SR-010	SR-PVD-010	1000	2.0	7.5	1.2	7.6	5.3	7658
SR-011	SR-PVD-011	500	2.2	11.7	1.3	10.4	9.0	7042

Figure 10 summarizes the key observations of the above studies, with inclusion of the silicon nitride reference film, for each susbtrate. ALD thickness was either 500 or 1000 angstroms. Also shown is the measurement for Cz and SR passivated with SiNx deposited in our R&R CVD reactor.

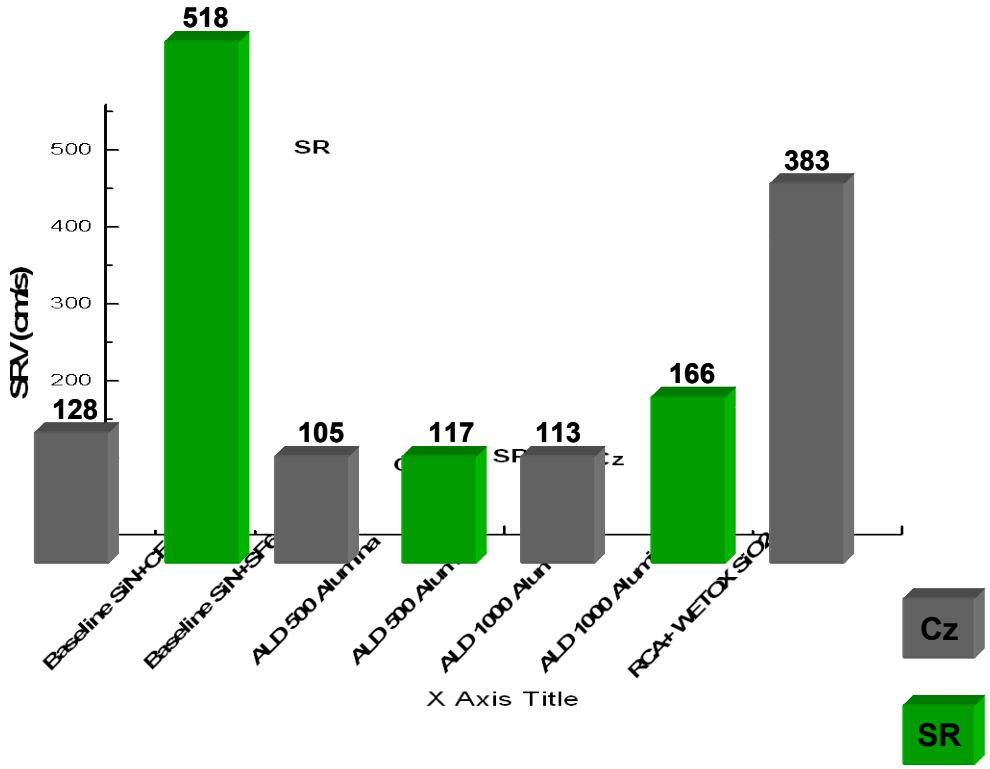

Figure 10. SRV (cm/s) versus film type, substrate and pre-process for the data tables.

By far, the most significant result of the above work is the performance of ALD alumina on SR wafers. Currently this is our lead candidate for surface passivation. We noted that there was not significant change in SRV following the heat treatment, which is significant for cell metallization steps following film deposition. Furthermore, since our SRV results clearly demonstrate that some form of pre-clean to remove surface contaminants is very beneficial for the majority of films, pre-clean will be part of the next ALD alumina studies. In light of the fact that our program objective for rear passivation is 100 cm/s, the results reported here indicate that we have made significant progress since our previous surface passivation results.

3. Next Steps: Passivating surface film stability

Over the coming months we will report on our results with passivating the surfaces with a variety of dielectric films, improved wafer clean processes, as well as stability of the surface passivation over time.

July

1 Efficiency improvement of string ribbon silicon solar cells with a Back Emitter Etch Junction Isolation

A new String Ribbon efficiency improvement program, based on a back emitter etch junction isolation design, was initiated in June. Here we summarize program objectives, research plan and some initial results.

1.1 Background

The present junction isolation (JI) for SR cells uses a laser scribe around the front surface of the cell. Laser scribing the front of the cell leads to improvement in FF, due to an increase in shunt resistance, R_{SH}, and a reduction in series resistance, R_S. This approach, however, has the limitation of reducing the short-circuit current I_{SC}, due to a reduction in effective cell area. One alternative JI scheme used by some cell manufacturers uses a wet process to chemically etch the back emitter. This process has the potential problem that some of the etch chemistry, either as the liquid or its vapors, can also attack the front emitter. At Evergreen we are developing a dry back emitter etch (BEE) process using a reactive chemical plasma.

2 Back Emitter Etch Processing

2.1 BEE Process Overview

Cell processing research discussed here uses production line GII String Ribbon wafers with an average wafer thickness of 190 μm and a p-type bulk resistivity averaging 3 Ω-cm. Processing begins with a dilute HF etch to remove a thin as-grown oxide. Wafers were textured in an inline process tool using chemistry described previously. Emitter formation by phosphorus diffusion employed a liquid $POCl_3$ source in a horizontal tube furnace, with process time and temperatures to achieve a mean sheet resistivity of 75 Ω/□. Junction depths are about 0.25 microns. Initial emitter etch work focused on establishing reactivity of etch gases and required etch times by etching wafers in the Roth & Rau AK800 reactive ion etch (RIE) tool. Reactive gases include SF_6 and CF_4, and etch rates were varied by dilution of the reactive gas with Ar. Other plasma tool conditions include plasma power of 2000W, 250V, 25mTorr. We also examined the use of ion bias. Emitter removal was established by depth and sheet rho mapping of the etched portions of the wafers while masking with sc-Si wafers. A typical etch result is shown in Figure 11. These data provide confirmation of emitter removal.

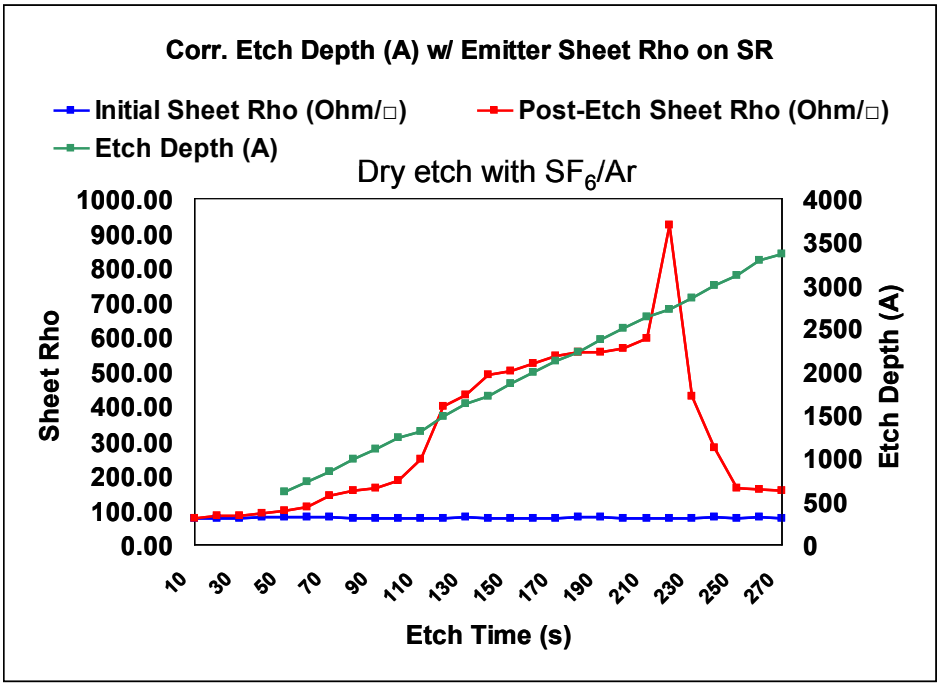

Figure 11. Depth profiling and sheet rho analysis to track emitter removal.

Early on we noted a phenomenon that suggests wrap-around of the plasma to the front side, as illustrated using SiN masked front surfaces. This effect is shown in Figure 12. This, of course, leads to front emitter removal, lower I_{SC} and potentially higher leakage current; similar to what is seen for a wet BEE process. One solution to this problem is to employ plasma shadow walls by creating a recess for the wafer to block ion attack of the front.

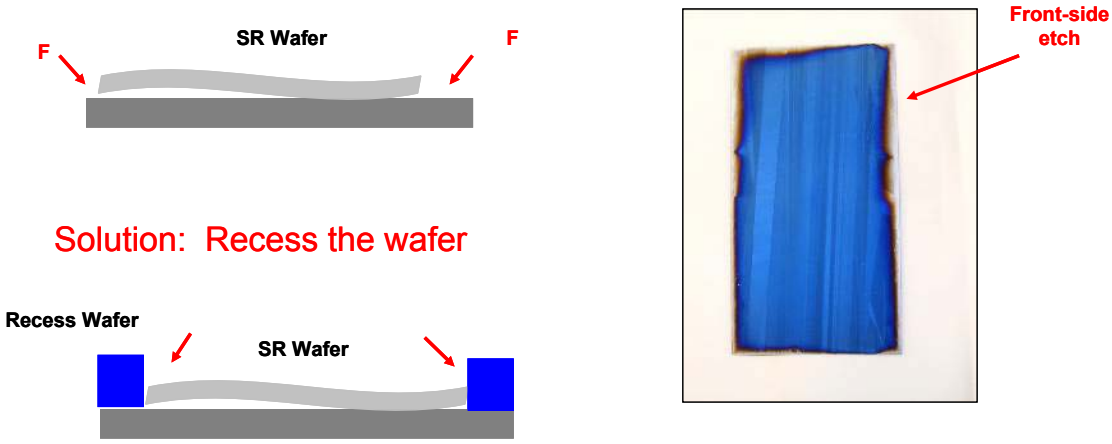

Figure 12. Schematic illustrating wrap-around of plasma etch (F^- ions) to the front of the cell. Front is coated with SiN.

We ran a process split design with several concepts to evaluate masking the front, in addition to using the

recess platen in the RIE tool. Mask material includes the PSG layer from the diffusion and/or a SiN deposition. Conditions for a typical BEE dry etch experiment included: 1) a control group (SOP laser JI process), 2) Wet Etch PSG on both sides; Dry Etch back emitter, 3) Front-side SiNx mask on PSG; Dry Etch back PSG and emitter, 4) Wet Etch PSG (both sides); dep. Front-side SiNx mask; Dry Etch back emitter, and 5) Dry etch back PSG and emitter; wet etch front PSG. Typical results for this experimental design are shown in Table 7. The splits 0-4 are described in the text. The last condition (split CD) is for a wet BEE process (Konstanz CI).

Table 7. Plasma etch experiment cell results.

Split	n	Split	%E	Voc (V)	Isc (A)	FF (%)	Rs	Rsh
0	17	SOP Cell Process	15.12	0.601	4.113	73.4	1.07E-02	72.8
1	8	PSG Etched	14.73	0.588	4.016	72.1	9.84E-03	101.2
2	8	SiNx Mask on PSG Etched	14.43	0.597	4.117	70.5	1.30E-02	102.2
3	8	PSG Mask	15.05	0.601	4.159	72.3	1.04E-02	101.8
4	5	SiNx Mask on PSG Masked	14.56	0.602	4.181	69.4	1.55E-02	67.3
CD	n/a	Konstanz CI	14.66	0.603	4.004	72.82	1.14E-02	114

The data are consistent with some front emitter etch for splits 1&2 and no front emitter etch for splits 3&4. Electroluminescence (EL, data not shown) of groups 3&4 confirmed that there was no etch wrap-around, while cells from splits 1&2 exhibited varying degrees of wrap-around. Furthermore, the SOP Isc of 4.113 A is boosted by the anticipated increase in active area (1.16%), from 4.113 to roughly 4.161 A, for splits 3&4.

3. Next Steps: Larger image size for BEE cell process

Next steps include increasing front image size for BEE process (wet or dry process) to reduce series resistance Rs and increase FF, and reporting on parallel BEE efforts using a wet process.

September

1. Efficiency improvement of string ribbon silicon solar cells using improved front silver paste

Here we report on cell efficiency improvements using improved screen-printable front Ag pastes. Comparison of pastes from three manufactures shows that cell efficiency can improve by as much as 0.34% absolute (2.3 % relative) with Ag paste that has improved conductivity and contact resistance.

2. Solar Cell Processing

2.1 Cell Process Overview

Cell processing research discussed here uses production line GII String Ribbon wafers with an average wafer thickness of 190 μm and a p-type bulk resistivity averaging 3 Ω-cm. Solar cell processing begins with a dilute HF etch to remove a thin as-grown oxide. Wafers were textured as in an inline process tool using chemistry described previously. Emitter formation by phosphorus diffusion employed a liquid $POCl_3$ source in a horizontal tube furnace, with process time and temperatures to achieve a mean sheet resistivitiy of 75 Ω/□. A single-layer antireflective (SLAR) SiN_x coating was deposited by PECVD, followed by screen printing back Al and drying. Front Ag contacts were screen-printed using a two busbar design with 35 fingers having 120 μm wide artwork. Targeted as-printed finger width is approximately 130 μm. Final finger width and height after firing was determined using a profilometer. Metallization was completed by co-firing in a belt furnace. Front surface laser junction isolation completes cell processing.

2.2 Evaluation and Optimization of New Ag Pastes

The current SOP Ag paste (DuPont PV147) was used as the control. All Ag pastes were printed in the same day using the same screen with print conditions adjusted to give approximately 130 μm print width for each paste. Cells were dried and a firing optimization was performed for each paste, including the control group. Firing optimizations used in the studies presented here examined different firing zone temperatures at the same belt speed (205 inches/min). In other studies belt speed was adjusted in addition to temperature to change the firing profile. Table 8 summarizes the results of paste comparisons for three experiments. Cell data in Table 8 are for each paste fired at its optimum temperature.

Table 8. **Summary comparison of solar cell parameters for front Ag pastes**

	Ferro 33-503	DuPont PV149	Heraeus CL80-8978	DuPont PV147
Efficiency (%)	15.72	15.62	15.39	15.38
Voc (V)	0.605	0.603	0.602	0.601
Isc (A)	4.138	4.126	4.125	4.086
FF(%)	75.55	75.38	74.41	75.14
Rs (mohm)	8.4	9.2	9.4	9.3

The Heraeus paste was comparable in overall efficiency to the control group PV147. Both DuPont PV149 as well as Ferro 33-503 Ferro gave a performance boost over PV147, with Ferro 33-503 giving the largest cell efficiency boost, 0.34% absolute, over the control group PV147. The boost was due to improvement in all cell parameters. The improvement in Isc is associated with narrower finger width after firing, despite

a similar print width. The FF improvement was examined more closely to understand improvements associated with contact resistance R_C as well as screen-printed Ag resistivity ρ.

Screen-printed Ag resistivity ρ was determined from the measured resistance of the finger network between the busbars, denoted R_{BB}, and the mean finger cross-sectional area using the relation ρ = R_{BB}*Area*35/length, where length of the fingers is 7.3 cm. Contact resistance R_C for the pastes was determined using the measurement of the resistance between pairs of fingers (also referred to as a TLM structure) of 1-cm wide strips cut from the solar cell. Resistivity and contact resistance for the best Ag pastes, along with the SOP paste, are shown in Table 2.

Table 9. Characterization of front Ag metallization for solar cells given in Table 8

Paste	R_{BB} (mΩ)	Width (μm) x Height (μm)	Cross-section (μm^2)	Rectangular height (μm)	Resistivity, ρ (Ω-m) $x10^{-8}$	Contact Resistance (mΩ-cm^2)
PV147	74	15 x 153	1545	10.1	5.46	7.4
PV149	62	26 x 118	2124	18.4	6.44	5.3
Ferro 503	48	24 x 116	1914	16.5	4.32	6.1
Ag					1.62	

A significant part of the better performance of Ferro 33-503 is its line conductivity, most likely due to the fact that it has the lowest glass content of the pastes studied. The lower glass content most likely leads to better sintering of the Ag particles. Contact resistance for both PV149 and Ferro 33-503 are lower than PV147. This is expected since both of these newer pastes have been formulated to provide lower R_C on higher sheet rho emitters. We also note that the newer DuPont paste, as well as the Ferro paste, result in a narrower finger than PV147 after firing, leading to higher Isc.

3. Next Steps: Multiple Busbar (>3) Cell Designs

Cell modeling results indicated that additional busbars, in excess of five, could achieve a substantial reduction in series resistance. For this reason, the next round of front grid optimization will examine additional modelling and experimental results for poly- or multi-busbar designs with as many as 31 busbars. Ferro 33-503 Ag paste performance parameters will be part of this round of modelling and cell processing.

October

1 Efficiency improvement of string ribbon silicon solar cells using optimized front grid design

Here we report on cell efficiency improvements using an optimized front metallization grid, including narrower fingers and multiple busbars. Modeling shows that an efficiency improvement of 0.6% absolute can be realized by reducing finger width and increasing the number of bus bars.

2 Solar cell Processing

2.1 Cell Process Overview

Cell processing research discussed here uses production line GII String Ribbon wafers with an average wafer thickness of 190 μm and a p-type bulk resistivity averaging 3 Ω-cm. Solar cell processing begins with a dilute HF etch to remove a thin as-grown oxide. Wafers were textured in an inline process tool using chemistry described previously. Emitter formation by phosphorus diffusion employed a liquid $POCl_3$ source in a horizontal tube furnace, with process time and temperatures to achieve a mean sheet resistivitiy of 75 Ω/□. A single-layer antireflective (SLAR) SiN_x coating was deposited by PECVD, followed by screen printing back Al and drying. The SOP cell groups employed a screen-printed Ag paste (Ferro 33-503) design of two busbars (2BB) with 35 fingers having 120 μm wide artwork. Metallization was completed by co-firing in a belt furnace. Front surface laser junction isolation completes cell processing.

2.2 Results and Discussion

Our initial proposed multiple busbar design was selected based on modeling using a resistive loss/shadow loss simulation. The results of this simulation are shown in Table 10.

Table 10. Resistive loss/shadow loss simulation of cell efficiency for multiple busbar designs.

Bussbars	# Fingers	Finger Width (um)	Eff (%)
11	51	60	16.00
13	50	60	16.02
15	50	60	16.04
17	49	60	16.04
19	49	60	16.03
11	44	80	15.87
13	43	80	15.90
15	43	80	15.92
17	42	80	15.92
19	42	80	15.91
11	40	100	15.75
13	39	100	15.79
15	39	100	15.81
17	38	100	15.80
19	38	100	15.80

For this simulation a 2BB simulation was first established for the 2BB control group. The multiple busbar simulation modifies the front metallization pattern of the 2BB model, using actual finger cross-section, pitch and busbar wires. Six-mil Ag plated Cu wire was used for the multiple busbar cells in the work reported here. The simulation shows that a 15BB or 17BB, 40 finger x 60 micron finger width should be optimal. Cells were screen-printed with a 15BB pattern on material similar to that used for the 2BB control group. The actual pattern printed (shown in Figure 13) consists of 40 fingers and 15 columns of circular pads (0.4 mm diameter) for solder attachment of the 6-mil busbar wire.

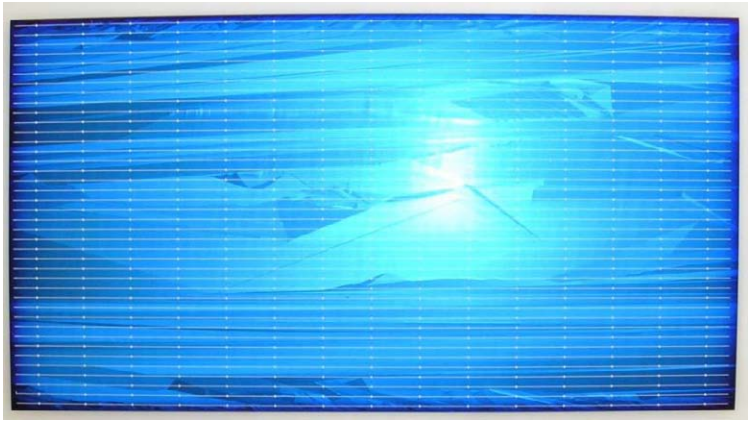

Figure 13. Actual 15BB cell before wire soldering.

Table 11 summarizes the cell data for the 2BB control group (25 cells) and the 15BB group (10 cells).

Table 11. Cell data for 2BB control and 15BB design.

Group	Efficiency (%)	Voc (V)	Isc (A)	FF (%)	Rs (mohm)	Shadow loss, incl. tabbing (%)
2BB	15.38	0.598	4.101	75.25	8.0	6.98
15BB	15.92	0.602	4.266	74.33	10.7	4.21

The boost realized for with this design is 0.54% absolute, which is somewhat less than the simulated boost of 0.66%. The multiwire design should have a somewhat lower Rs, and consequently higher FF, than realized in this experiment. Nonetheless, a boost of the magnitude realized here, achieved by means of a more optimized resistive loss/shadow loss, is quite substantial, and demonstrates the potential of this type of cell design.

3. Next Steps: Optimization of the Multiple Busbar Design

The next round of front grid optimization will examine additional cell builds of other simulation designs shown in Table 10 to explore the fidelity between our multiple busbar cell process with the cell simulation..

November

1. Efficiency improvement of string ribbon silicon solar cells using optimized front grid design: Part II

Following our initial efforts with building multiple busbar cells with a single design (15 busbars) we have developed a more streamlined, consistent build process that ensures more reliable and consistent wire soldering, which is reported here. We also report on evaluation of other multiple busbar designs, in particular, cell performance as a function of the number of busbars.

2. Solar cell Processing

2.1 Cell Process Overview

Cell processing research discussed here uses production line GII String Ribbon wafers with an average wafer thickness of 190 μm and a p-type bulk resistivity averaging 3 Ω-cm. Solar cell processing begins with a dilute HF etch to remove a thin as-grown oxide. Wafers were textured in an inline process tool using chemistry described previously. Emitter formation by phosphorus diffusion employed a liquid $POCl_3$ source in a horizontal tube furnace, with process time and temperatures to achieve a mean sheet resistivitiy of 75 Ω/□. A single-layer antireflective (SLAR) SiN_x coating was deposited by PECVD, followed by screen printing back Al and drying. The SOP cell groups employed a screen-printed Ag paste (Ferro 33-503) design of two busbars (2BB) with 35 fingers having 120 μm wide artwork. Metallization was completed by co-firing in a belt furnace. Front surface laser junction isolation completes cell processing. Cells were tested using a probe station to make electrical contact along the full length of the busbar with minimal shading. Contact to the back of the cell was accomplished with a similar number of probes (vacuum holds cell in place).

Multiple busbar cells were printed using the same screen-print process as that used for the SOP cells. Cells were then co-fired and laser junction isolated. Currently we have no means of reliably testing these cells without soldering of the wires. To do this, solder paste (Sac305, AIM Solder) is printed onto the Ag solder pads using an 8-mil thick SS stencil. The amount of solder paste per solder pad has not been fully optimized. A loom holding the 6-mil busbar wire is then aligned to the columns of solder pads and pressed against the cell, which is then heated from below (resistive heater) and from above (IR lamp) (Figure 14).

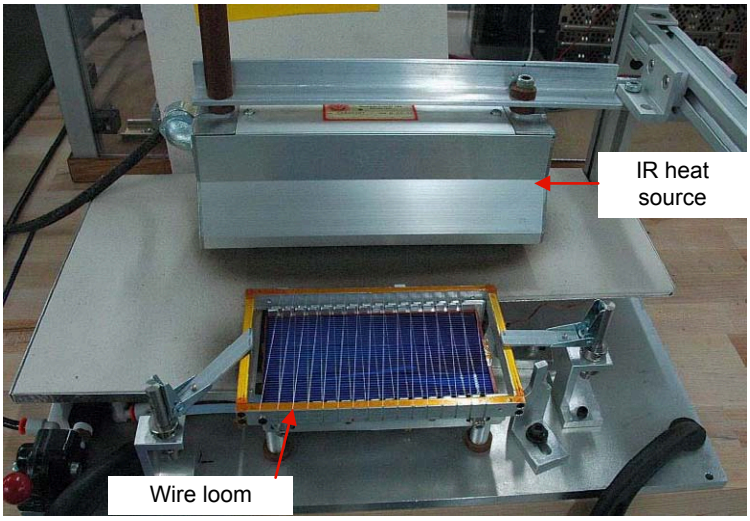

Figure 14. Wire soldering jig illustrating attachment of busbar wires.

Once the cell is cool a crosstie is attached to the wires along one side and the excess wire is removed. The cell is now ready for test. Testing is done in the same solar simulator used for the SOP cells, except the top probe fixture is removed and a clip is attached to the crosstie for front contact. Other details comparing the differences between testing of SOP and multiple busbar cells will be discussed in a later report.

2.2 Results and Discussion

Multiple busbar cells were fabricated with 15, 19, 23, 27 and 31 busbars. The SOP cell group for the present study is the same as that reported previously (October 2007 Monthly Report). Simulation of the cell performance of multiple busbar designs used the resistive loss/shadow loss model described previously. The results of this simulation are shown in Table 12, along with the actual cell efficiencies for these designs. The results are plotted in Figure 15.

Table 12. Optimization of BB count for MW design, simulated and experimental data.

Buss bars	# Fingers	Finger Width (um)	Simulated Eff (%)	Actual Eff (%)
11	40	60	16.04	NA
15	40	60	16.07	15.92
19	40	60	16.06	15.93
23	40	60	16.03	15.90
27	40	60	15.99	15.72
31	40	60	15.94	15.80
37	40	60	15.84	NA

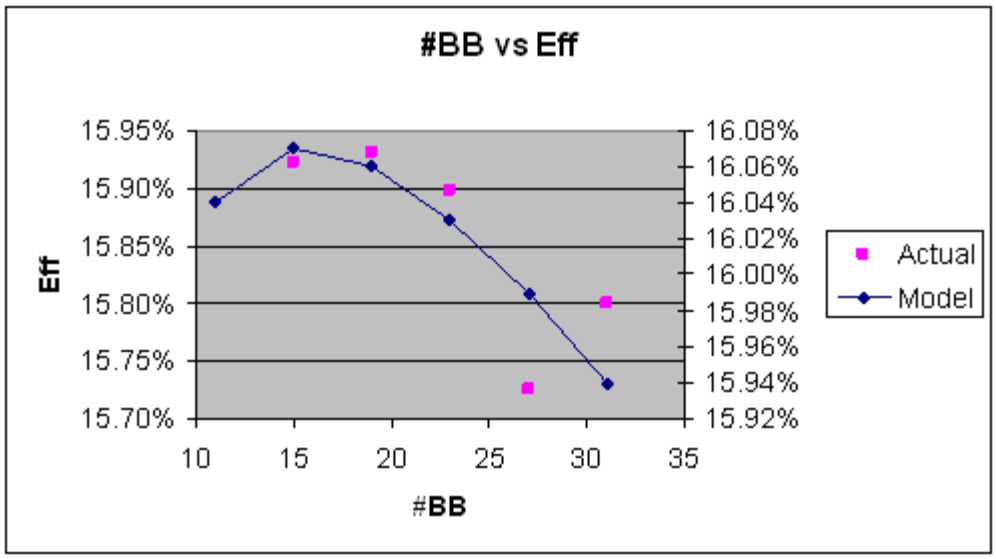

Figure 15. Plot of actual and simulated efficiency for MW BB study.

Note the different scales. See below for an explanation of 27BB data.
Table 13 lists all cell parameters for the multiple busbar and SOP cells.

Table 13. Cell data for MW BB optimization, 40 x 60 finger pattern.

BB Count	Efficiency (%)	Isc (A)	Voc (V)	FF (%)	Rs (ohms)
2 (SOP)	15.38	4.101	0.598	75.25	8.0
15	15.92	4.237	0.600	75.11	8.6
19	15.93	4.227	0.601	75.31	8.4
23	15.90	4.200	0.600	75.76	7.6
27	15.72	4.171	0.599	75.47	8.0
31	15.80	4.158	0.599	76.15	7.1

The data reported in Table 13 indicate a boost over the 2BB control group of 0.55%, and are similar to the best MW design seen earlier with this material and reported in October 2007 Monthly Report. These results demonstrate that we can repeat the 0.5-0.6% boost with MW design, as well as illustrate the good fidelity between the model behavior and realized cell performance. The 27BB cells had wire soldering issues, leading to higher Rs, lower FF, than expected for this group.

3. Next Steps: Leveraging Multiple Busbar Design for Higher Sheet Rho

One potential area of opportunity for higher cell efficiency is to reduce the emitter thickness for better cell blue wavelength response. Our studies in this area lead to increasing emitter sheet resistivity from 45 ohm/square to its current level of 75 ohms/square, with roughly an attendant increase in cell efficiency of about 0.3% absolute with a 2BB cell design. Efforts to increase cell efficiency further, by increasing sheet resistivity above 75 ohms/square, however, have been thwarted by too large a drop in FF without further increasing finger count. However, this had resulted in lower cell efficiency due to too much shading by the wide fingers needed in this 2BB design. It is possible, however, with the finer finger capability of the multiple busbar design, to increase finger count modestly to accommodate the higher sheet rho yet add only slightly to shading loss. The net result, in principal, should be better blue response (increasing I_{SC}) with only a slight increase in shading, for higher overall cell efficiency.

December

1. Efficiency improvement of string ribbon silicon solar cells using Higher Sheet Resistance Emitters

One potential opportunity for higher cell efficiency is to reduce the emitter thickness for better blue wavelength response. Here we report on the advantage of the finer finger capability of the multiple busbar design to increase finger count to accommodate the higher sheet rho yet add only slightly to shading loss. The net result, in principal, should be better blue response (increasing J_{SC}) with only a slight increase in shading, for higher overall cell efficiency.

1.1 Background

Previously we reported progress with higher sheet rho emitters using a 2BB metallization scheme. Those results are repeated here for purposes of comparison with the multiple busbar design. The phosphorus emitter diffusion was studied to improve J_{SC} of the solar cell by improving the blue response. The intention was to minimize heavy-doping effects in the emitter associated with a 40-50 Ω/□ emitter and to reduce emitter saturation current density J_{oe}, leading to higher J_{SC} and V_{OC}. Our current cell process uses a homogeneous emitter design, however, so the optimization of sheet resistivity includes improving J_{SC} without reducing FF. Initial optimization of the emitter sheet rho was performed using non-textured String Ribbon wafers diffused in a low-pressure Semco $POCl_3$ tube furnace in the sheet rho range from 55 to 90 ohms/sq. Either Toyo or Ferro Al paste was printed on the back and DuPont PV 147 Ag paste was printed on top of the SiN_x using a 35-finger pattern of 120 μm-wide fingers. Optimization of Al and Ag co-firing was performed using a five-zone SierraTherm belt furnace. An initial screening experiment for this process is shown in Table 14.

Table 14. Cell Parameters for sheet rho study (approximately 35 cells per group)

Sheet rho (Ω/□)	V_{OC} (mV)	I_{SC} (A)	FF (%)	Eff (%)
55	605	3.842	75.24	14.60
75	604	3.904	74.54	14.66
85	605	3.928	74.02	14.66
95	606	3.950	72.23	14.41

While it is not expected that the same finger count will provide an optimal FF for the range of sheet resistivities studied here, this experiment demonstrates 1) the expected improvement in J_{SC} for higher sheet rho emitters, and 2) the possibility of fabricating reasonable screen-printed contacts to higher sheet rho emitters with a commercial Ag paste. Lack of improvement in V_{OC} with higher sheet resistivity suggests that the SiN surface passivation is inadequate to support a reduction in J_{oe}. In a subsequent optimization of finger count on 55, 75 and 90 Ω/□ showed that the best two busbar (2BB) finger pattern on 55 Ω/□ is 31 fingers, 120 μm wide (31 x 120), the best on 75 is Ω/□ is 35 x 120, and 37 x 120 is best on 90. Even with 37 finger count, there was still significant drop in FF at 90 Ω/□, associated with higher contact resistance (data not shown), such that cell efficiency drops off in going form 75 to 90 Ω/□. These data suggest that

the best cell efficiency opportunity with a more shallow emitter is in going from 55 to 75 Ω/□. Subsequent experiments using the optimized finger patterns on the respective emitters demonstrated an average efficiency boost of about 0.15% for 75 over 55 Ω/□.

The data shown in Table 14 are plotted along with a PC1D model of I_{SC} as a function of sheet resistivity in Figure 16. The poor fidelity between the PC1D model and the realized I_{SC} is in part due to the fact that a simple single error function is used to model the phosphorus emitter in PC1D, while the actual phosphorus emitter is characterized by a double error function. One goal of our higher cell efficiency effort is to develop a better understanding of how to more accurately model our cell, including sheet rho, inhomogeneous lifetime effects, and front and rear surface recombination.

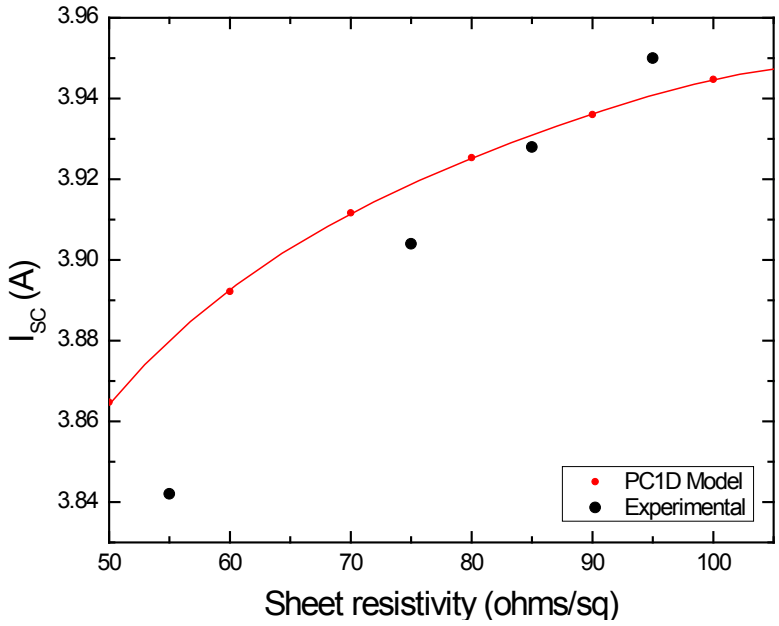

Figure 16. Plot of actual and PC1D modeled I_{SC} versus emitter sheet resistivity.

In the following section we apply the multiple busbar front grid as a more optimal cell design for high sheet resistivity, compared to the 2BB grid employed thus far.

2. Solar cell Processing

2.1 Cell Process Overview

Cell processing research discussed here uses production line GII String Ribbon wafers with an average wafer thickness of 190 µm and a p-type bulk resistivity averaging 3 Ω-cm. Solar cell processing begins with a dilute HF etch to remove a thin as-grown oxide. Wafers were textured in an inline process tool using chemistry described previously. Emitter formation by phosphorus diffusion employed a liquid $POCl_3$ source in a horizontal tube furnace, with process time and temperatures to achieve a mean sheet resistivity of either 75 or 90 Ω/□. A single-layer antireflective (SLAR) SiN_x coating was deposited by PECVD, followed by screen printing back Al and drying. The SOP cell groups employed a screen-printed Ag paste (Ferro 33-503) design of two busbars (2BB) with 35 fingers having 120 µm wide artwork. Metallization was completed by co-firing in a belt furnace. Front surface laser junction isolation completes cell processing.

Multiple busbar cells were printed using the same screen-print process as that used for the SOP cells. Cells were then co-fired and laser junction isolated.

2.2 Results and Discussion

Multiple busbar cells were fabricated on 75 Ω/☐ using the 15 busbar pattern (40 fingers, 60 micron artwork; 15BB 40 x 60) reported in the November 2007 Monthly report. In addition, we fabricated cells with this and other designs (15BB 50 x 60, 17BB 42 x 80 and 19BB 49 x 60) on 90 Ω/☐ cells. Firing optimizations were done separately on 75 and 90 Ω/☐ and indicated that 870 °C is optimal for both groups. Cell efficiency results comparing cell performance for 75 and 90 Ω/☐ groups are shown in Figure 17.

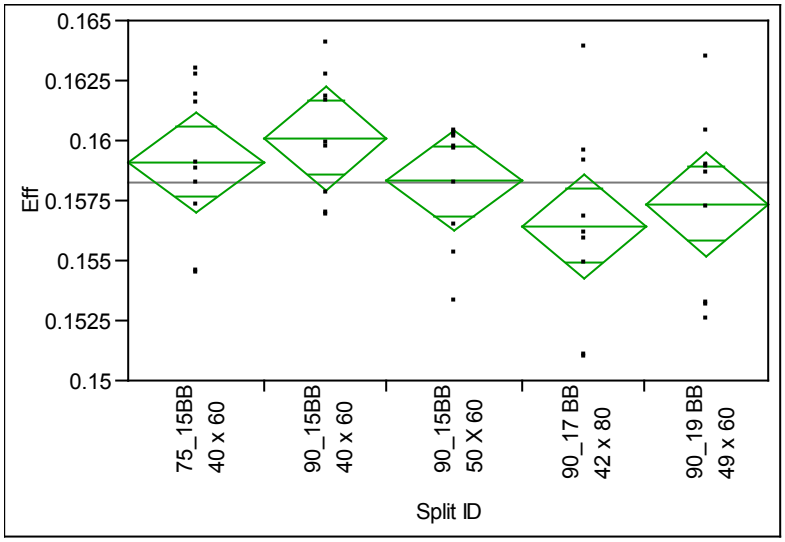

Figure 17. Cell efficiency for 75 and 90 Ω/☐cells with different MW front metallization designs.

All cell data are reported in Table 15.

Table 15. Cell data for MW BB designs on 75 and 90 Ω/☐.

Sheet resistivity (Ω/☐)	MW Grid	Efficiency (%)	Isc (A)	Voc (V)	FF (%)	Rs (mohms)
75	15BB 40 x 60	15.91	4.227	0.602	75.03	9.1
90	15BB 40 x 60	16.01	4.247	0.603	75.04	9.5
90	19BB 50 x 60	15.83	4.170	0.604	75.41	9.1
90	17BB 42 x 80	15.64	4.168	0.601	74.93	10.1
90	19BB 49 x 60	15.73	4.160	0.602	75.37	9.2

The data reported in Table 15 indicate a slight efficiency boost, about 0.1%, was realized with the 90 Ω/☐ group compared with the 75 Ω/☐ cells. This improvement seen with the MW design is noteworthy, since the 2BB design resulted in a decrease in cell efficiency in going from 75 to 90 Ω/☐. As expected, the boost is associated with higher current, with a drop in FF. This work needs to be repeated with considerably larger groups for each sheet resistivity (about 200 cells per group) to establish more reliable statistics.

The FF/I_{SC} trade-off between different designs deserves some comment. It was expected that the 17BB design would have had at least as good a FF as the 15BB 40 x 60 group (75.04%), though it was somewhat lower than this, at 74.93%. Most likely there was some problem with this group, such as less than ideal finger printing. Otherwise, designs with more fingers had the expected outcome, leading to higher FF and lower I_{SC}.

3. Next Steps: Non-Contact Printing

One potential opportunity for higher cell efficiency is to use non-contact printing (NCP) to improve finger print quality over screen-print quality. An even more significant benefit with NCP should be cell yield, especially as the cell thickness is decreased from our current thickness of 190 microns to 150 microns.

Section 2- COTF

This section describes a chronology of events during the year with regard to cut-on-the-fly (COTF) process improvements (Task 3.11).

January

This month we continued to make improvements to the In-Situ Ribbon Cutting System by making improvements to the thickness control on the wafer. Figure 18 shows the range of thicknesses that can occur within a population of wafers. Getting better control of this variation will reduce the requirements for the laser. The specific improvements this month include:

1. Improve thickness scanner performance to control wafer weigh. The primary effect of this is to reduce the variation in the center of the wafer.

2. Gain better control on the gas flow used to control edge thickness. Our Quad furnace design uses gas jets to thicken the edges of the wafers to increase the thickness. Unfortunately, the thickness of the wafers at the edges varies, and in some cases the thickness is so high that the laser doesn't cut all the way through the wafer. As the wafer is moved at the end of the cutting process, the portion that was not completely cut through typically breaks creating a mouse bite. The goal of adjusting the gas jets is to ensure a more uniform edge thickness that is consistent with the laser cutting capabilities.

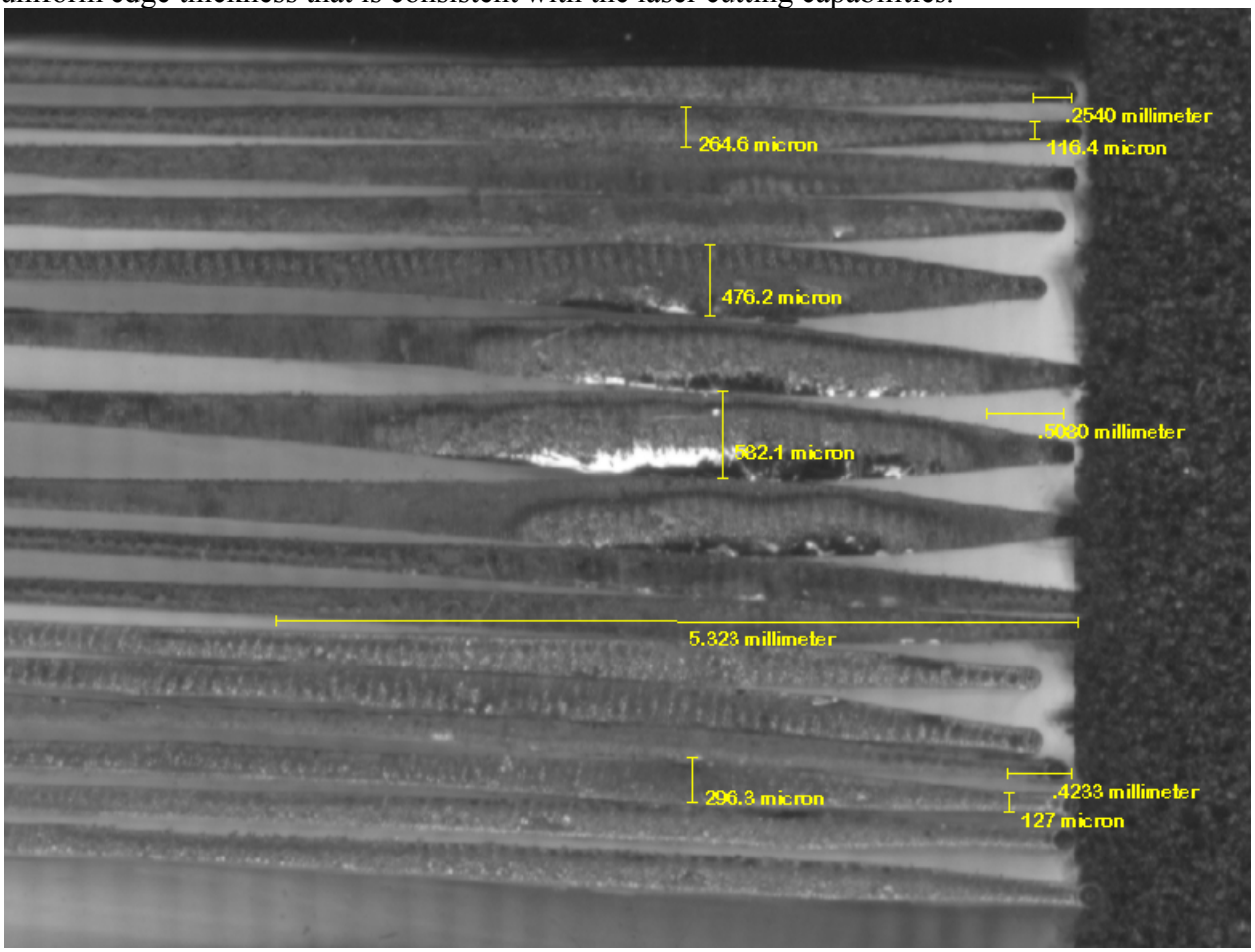

Figure 18. Thickness Variations in Wafers

February

This month was spent characterizing the capability of the COTF system to meet our wafer fabrication size specification. The size specification is 80.5 +/-1.4 mm. The data in the Figure 19 show wafers from both the results of manual cut wafers (labeled as Gemini) as well as wafer fabricated with the COTF system (labeled QUAD). The quad wafers have a mean of 80.4 mm with a standard deviation of 0.196 mm. These wafers more than meet the specification, as the three sigma value is 0.6 mm which is well within the 1.4 mm tolerance. Note that this is a significant improvement over the manual system which has a standard deviation of 0.31 mm. Based on these results, we have concluded that no additional work is required in this area.

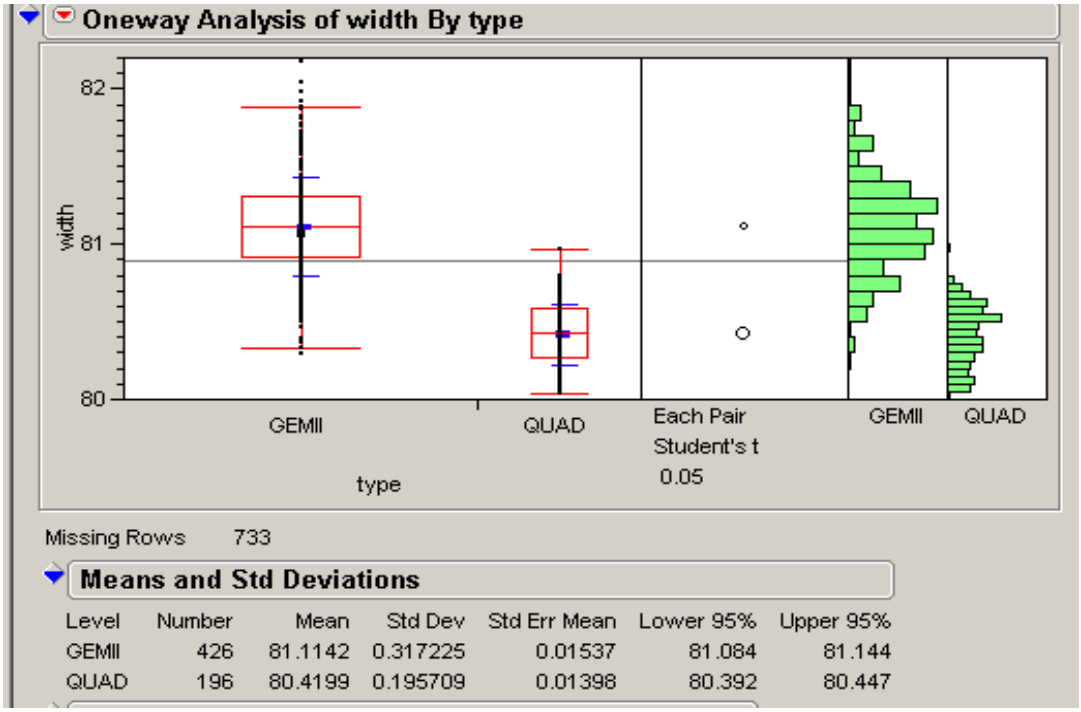

Figure 19. Distribution of wafer lengths for COTF system

March

This month, we initiated an effort to reduce the cost of the laser used in the In-Situ Ribbon Cutting System. The driver for this effort is primarily cost reduction, which is essential for the long-term production viability of the technology. The first production release of the technology relied on a commercially available laser system that we purchased from Rofin, a German laser manufacturer. The laser is intended as a stand alone system. As such it has many features that are not required for our application, but that contribute significantly to the cost of the system.

Our plan is to replace the Rofin laser with a system custom designed for our application. The plan calls for saving cost by (1) using a smaller galvo for directing the beam; (2) using a smaller focusing lens; (3) elimination of a hard drive; and (5) 24 volt operation for the PC, which eliminates the need for a power transformer. The plan calls of using the same fiber laser, which is supplied to Rofin by IPG. The major

engineering challenge is the design of optical system. Figure 20 shows a schematic diagram of the optical system, with the key elements identified.

The main work completed this month includes completion of the optical design and assembly of a bench top system that will be used next month to evaluate the system performance. Figure 21 shows the bench top system.

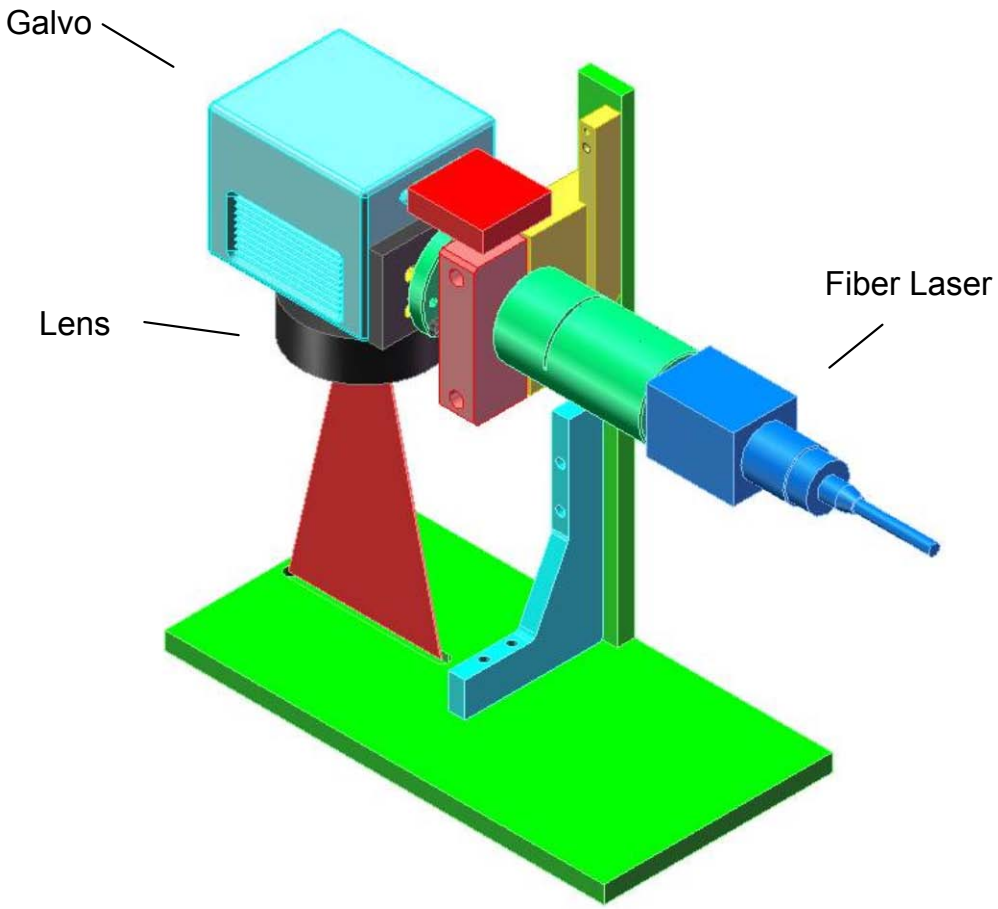

Figure 20. Schematic diagram of new laser system

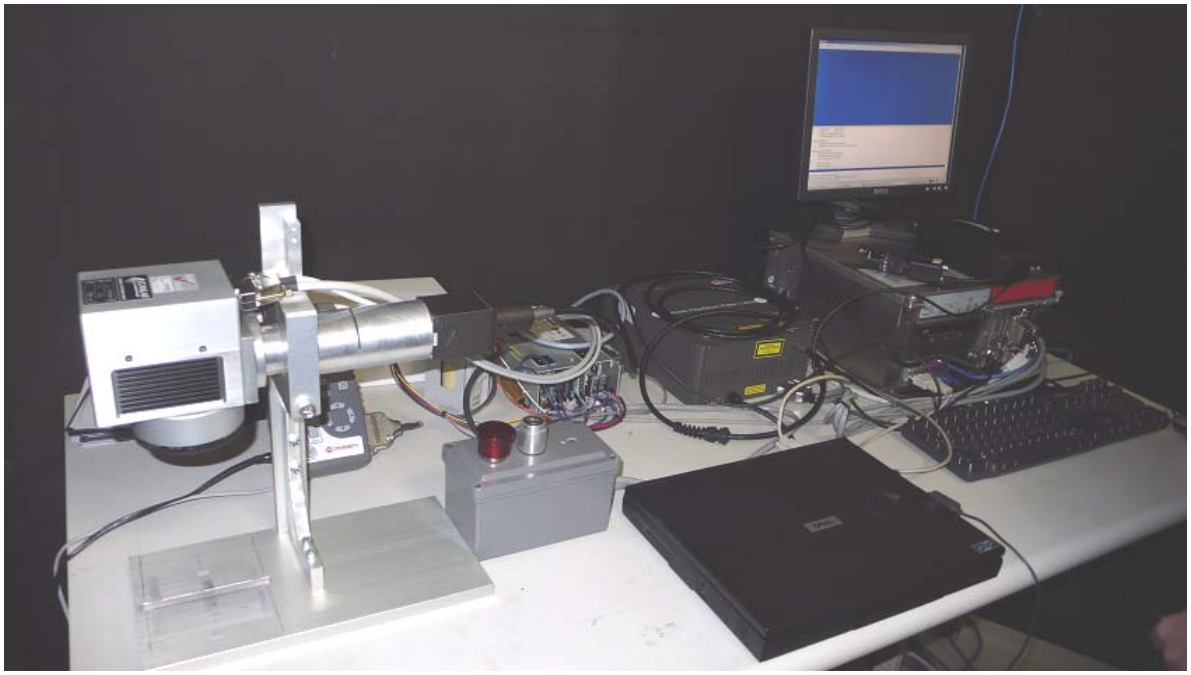

Figure 21. Photograph of Bench Top System

April

This month much of the work on the cut-no-the-fly system focused on designing a means to retrofit the existing furnace system with the newly designed low cost laser. Figure 22 shows the design of the retrofit.

The key elements for retrofit are:

1. A control box, which contains the electronics for driving the fiber laser;
2. The IPG fiber laser—the same fiber laser used in the Rofin laser
3. An industrial PC, that controls the electronics and the galvo;
4. A light shield to prevent leakage of the laser light

In the Rofin system, that we are working to replace all of these elements were contained within the laser system enclosure that sat where the control box sits in this system.

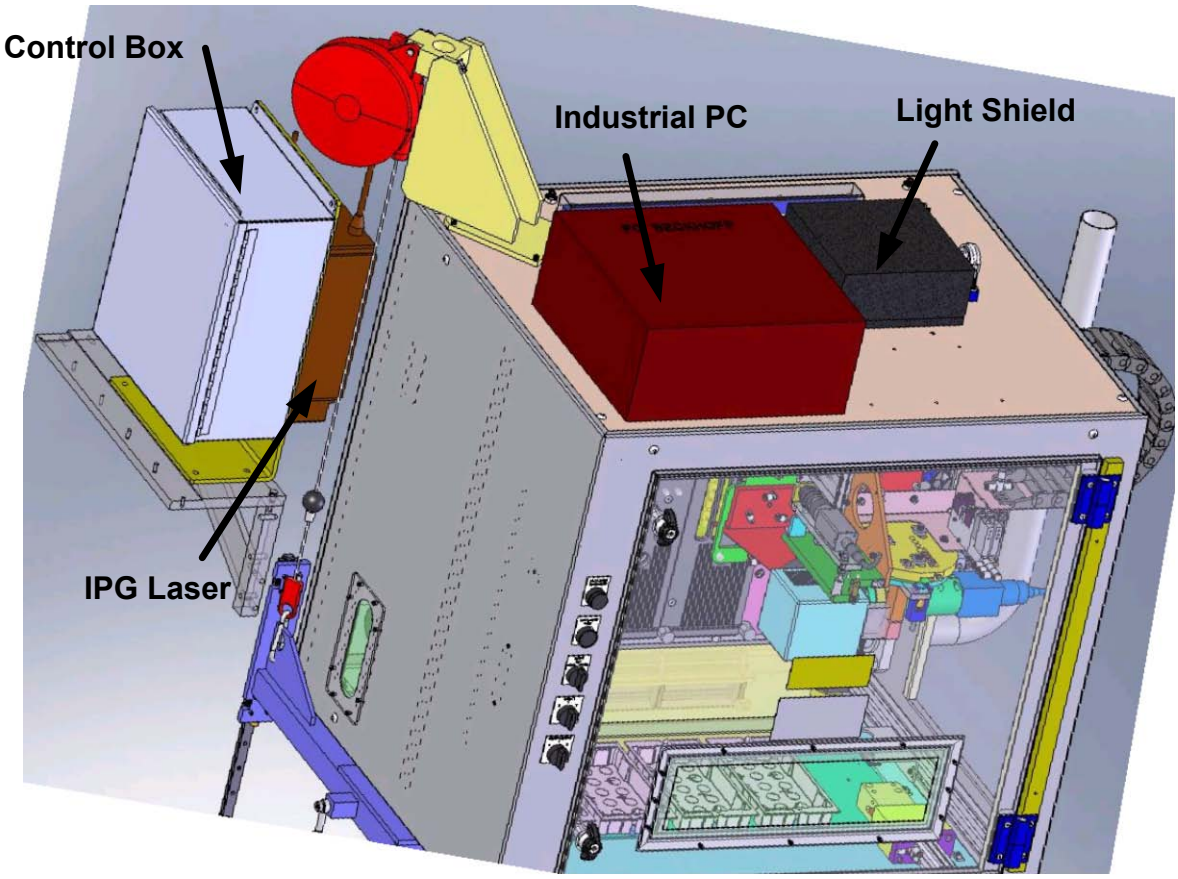

Figure 22. Schematic of New Laser Retrofit for Quad Mesa Furnaces

May

The work this month on the COTF system consisted on installing the new laser design on one of the QM3 furnaces and initiating the debugging process. The major activities for the month consisted of:

1. Testing the laser software and the integration of the laser and furnace software. Several bugs were identified and resolved.

2. Testing the alignment of the ATS laser. This effort revealed that the impact of the decision to use a smaller and less expensive galvo for beam steering in the new system. In particular, the ATS laser system is much more sensitive the beam size leaving the fiber laser. If the alignment is not perfect, the beam will be cropped, reducing power. This problem was remedied by working with IPG, the laser manufacturer and specifying a maximum beam size for the laser.

Once these minor design issues were resolved, we were ready to install three additional systems in the pilot line for a volume manufacturing evaluation.

June

This month we installed the new ATS laser system on a total of three quad furnaces and began initial evaluation of their performance. Figure 23 shows wafer fab yield for the three furnaces. The results are not significantly different from the furnaces with the previous laser system. The data for C21 and C09 show the date of transition to the new laser. C21 was run with the new laser for the entire period.

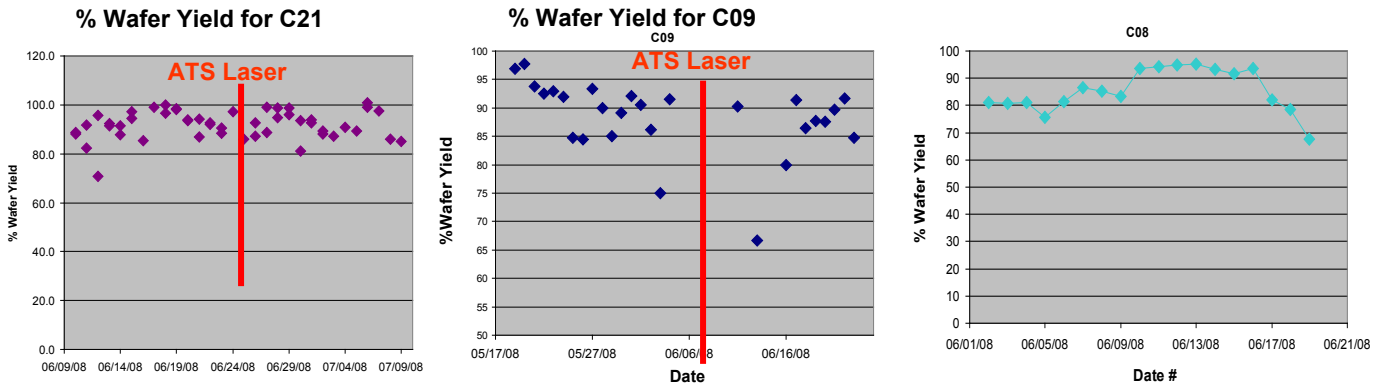

Figure 23. Wafer yield for furnaces C21 and C09, and C08 which have new ATS laser system.

July

No significant progress was made on this task this month.

September

Work this month has focused on debugging several design issues in the Cut on the Fly system. The specific issues addressed include:

1. Testing the Omron sensor that is used to detect the presence of a ribbon and initiate the cutting sequence;

2. Redesigning the back light to improve edge detection and increased edge detection speed. This issue is critical to ensure that the system can keep with growth as growth speeds are increase;

3. Redesigning the graphite back plate to reduce the amount of silicon that builds up on the plate from contact with the wafers;

4. Updating the software to reduce the number of errors that require manual cuts.

5. Modifying the pitch of the screw on the vertical translation stage to match the cut-head speed to the ribbon puller speed. This eliminates any difference in speed between the cut head and ribbon while the ribbon is being gripped.

October

We have continued to evaluate the performance of the prototype Cut On the Fly (COTF) Systems. The goal of this effort is to identify equipment issues and resolve them to improve the productions worthiness of the system. Figure 24 shows the uptime for the quad systems with the COTF system for August and September. Note that there was a significant drop in late September that was attributed to COTF failures.

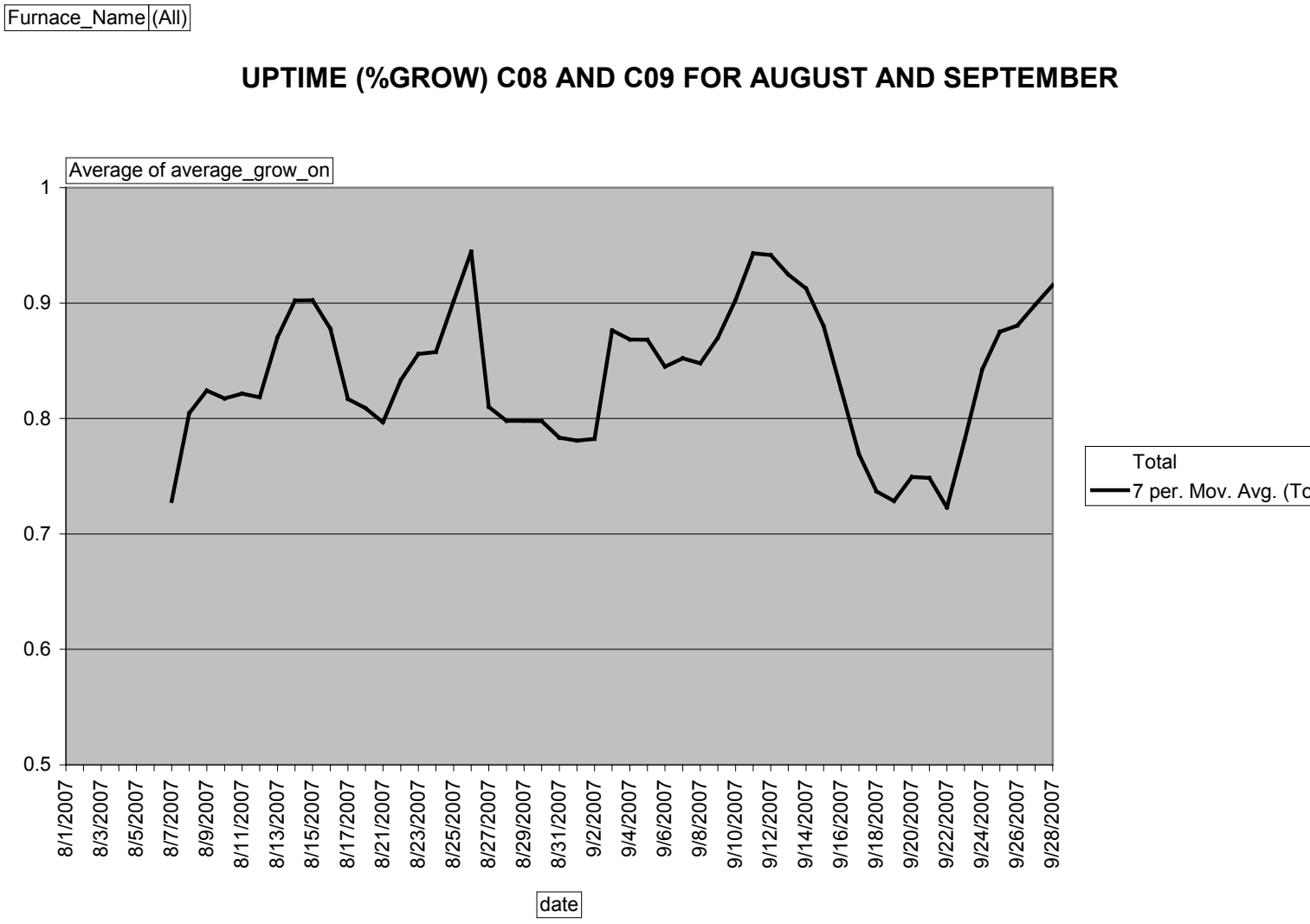

Figure 24. Uptime data for Quad Ribbon Growth Furnaces with COTF

Much of the team effort this month was spent debugging some of the issues that had caused the downtime issues. The issues addressed included:

1. The ribbon detector sensor that was originally included in the design has proven unreliable. It was replaced with a comparable sensor from Omron.
2. The backlighting system was redesigned to improve the edge detection and to improve the scan rate.
3. The graphite back plate that the wafer is held against during cutting was redesigned to reduce silicon build up.

4. Several improvements were made to the software to reduce the number of manual cuts required.
5. The screw pitch on the translation stage that moves the cut head was changed to match the screw drives on the pullers. This will ensure that the head moves at the exact same rate.

Work for next month will continue to observe failures and effect design changes to make improvements.

November

Work this month on the In-Situ Ribbon cutting focused on reducing yield loss. The work centered on two efforts:

1. Reduce number of "manual cuts" and modify routine to reduce the amount of material thrown away when a manual cut happens. There are numerous sources of manual cuts. This work will seek to identify each of them.

2. Improve cutting performance by centering the wafer to eliminate mouse bites. Mousebites are currently running at 0.9 percent. Our goal is to reduce this less than 0.5 percent. Mouse bites occur when the laser does not cut completely through the edges of the wafer. The wafer then breaks at the edge. This is partly due to the alignment between the wafer and the laser, which is set up to accommodate the thicker wafer edges. Figure 25 shows the origin of a mouse bite.

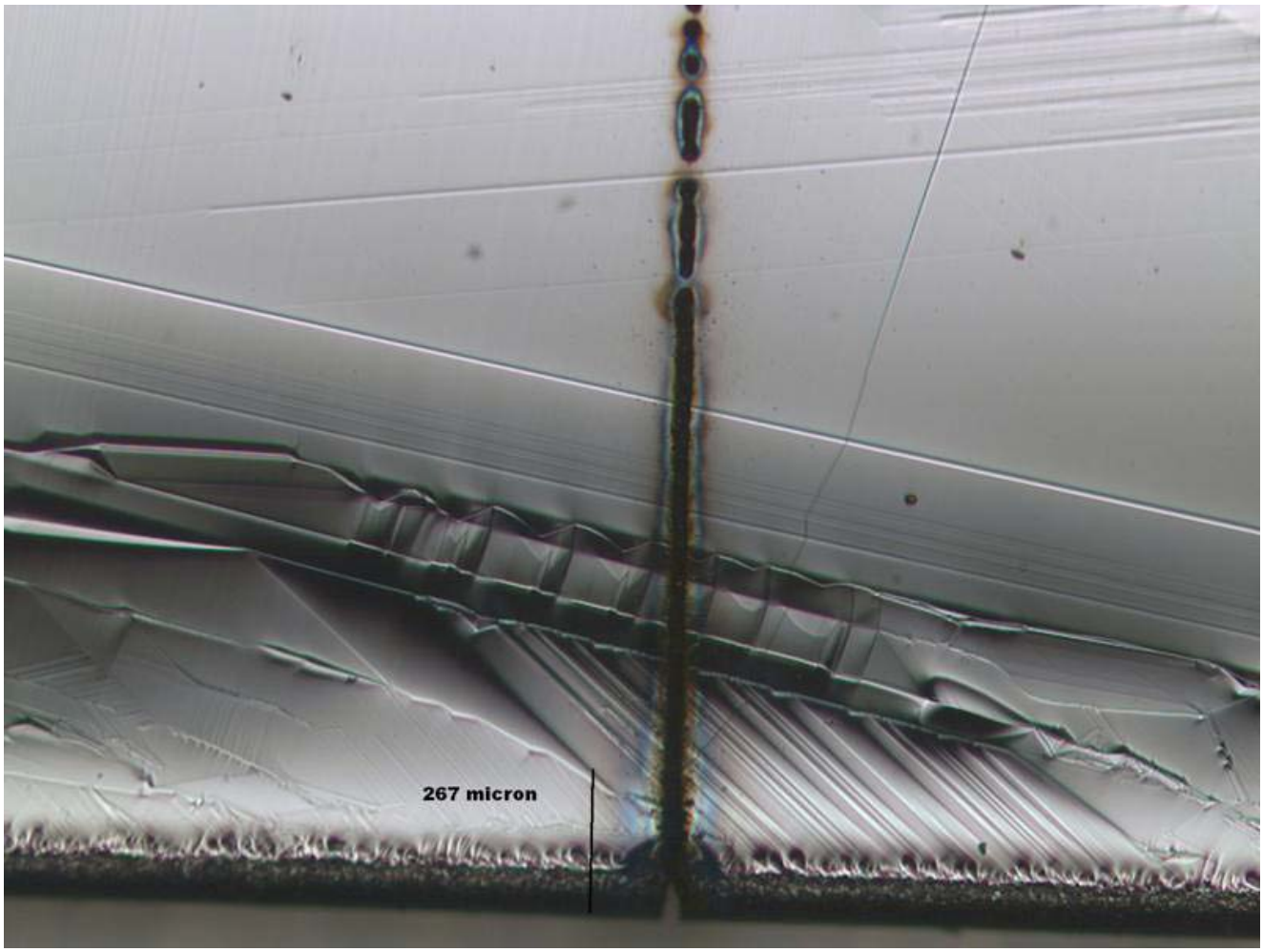

Figure 25. An incomplete cut through the thick portion of the wafer, which leads to a mouse bite in production

December

We have recently completed a four week campaign to assess the yield performance of the Quad 4.1 String Ribbon Growth Furnaces. One of the important leanings from the campaign is the performance of the In-Situ Ribbon Cutting System, which is also known Cut-on-the-Fly (COTF). The Campaign consists of running two furnaces for 28 days under production control. The Figure below shows the pareto of yield loss for the campaign. The purple bars represent the actual defect rate, while the blue bars represent our target rates. The following categories are, at least in part due to the COTF system:

- COTF/Lost Missing - This bin reflects wafers that enter the COTF system but don't make it to the Semi-Automatic Inspection System. There are several root cause for this failure, including wafers broken in the system and wafers that are not separated from the ribbon on the first cut. At this time, we don't have a full understanding of these loss mechanisms.

- MB (Mouse Bites) = This bin consists of wafers that have small defects at the edges. The mouse bite typically consists of a corner of the wafer that is broken off. We believe that this mechanism is primary due to incomplete cutting at the wafer edges, which are typically thicker than the rest of the wafer.

We plan to investigate both of these mechanisms over the next few months, aiming to reduce the defect rates to levels that are acceptable for production.

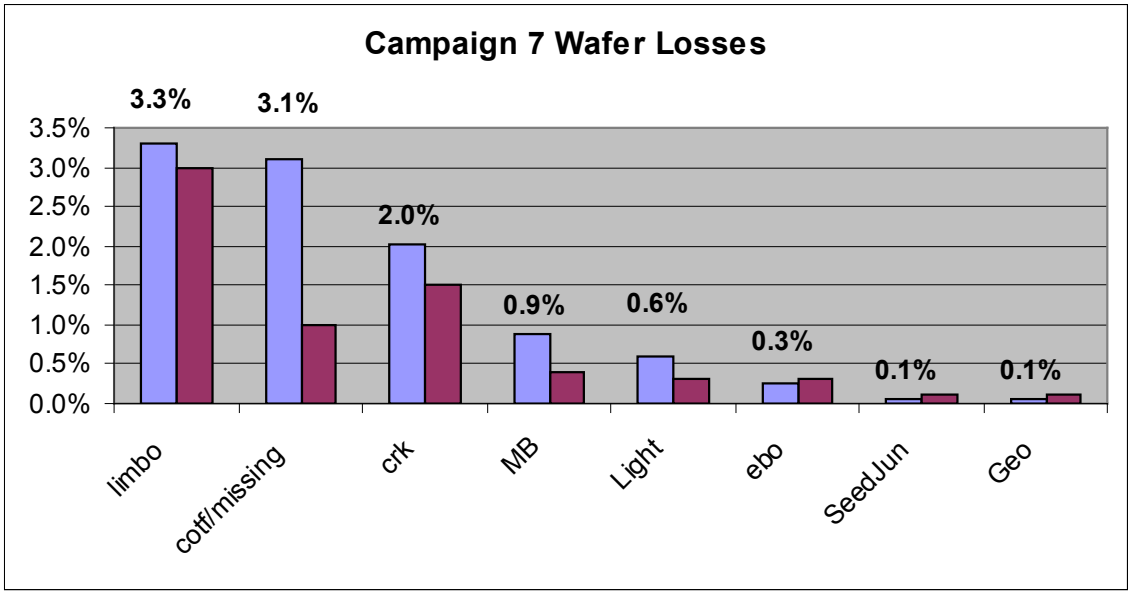

This month we continued to make improvements to the In-Situ Ribbon Cutting System. This month the effort focused on making improvements to the thickness control on the wafer. Figure 26 shows the range of thicknesses that can occur within a population of wafers. Getting better control of this variation will reduce the requirements for the laser. The specific improvements this month include:

- Improve thickness scanner performance to control wafer weigh. The primary effect of this is to reduce the variation in the center of the wafer.

- Gain better control on the gas flow used to control edge thickness.

  Our Quad furnace design uses gas jets to thicken the edges of the wafers to increase the thickness. Unfortunately, the thickness of the wafers at the edges varies, and in some cases the thickness is so high that the laser doesn't cut all the way through the wafer. As the wafer is moved at the end of the cutting process, the portion that was not completely cut through typically breaks creating a mouse bite. The goal of adjusting the gas jets is to ensure a more uniform edge thickness that is consistent with the laser cutting capabilities.

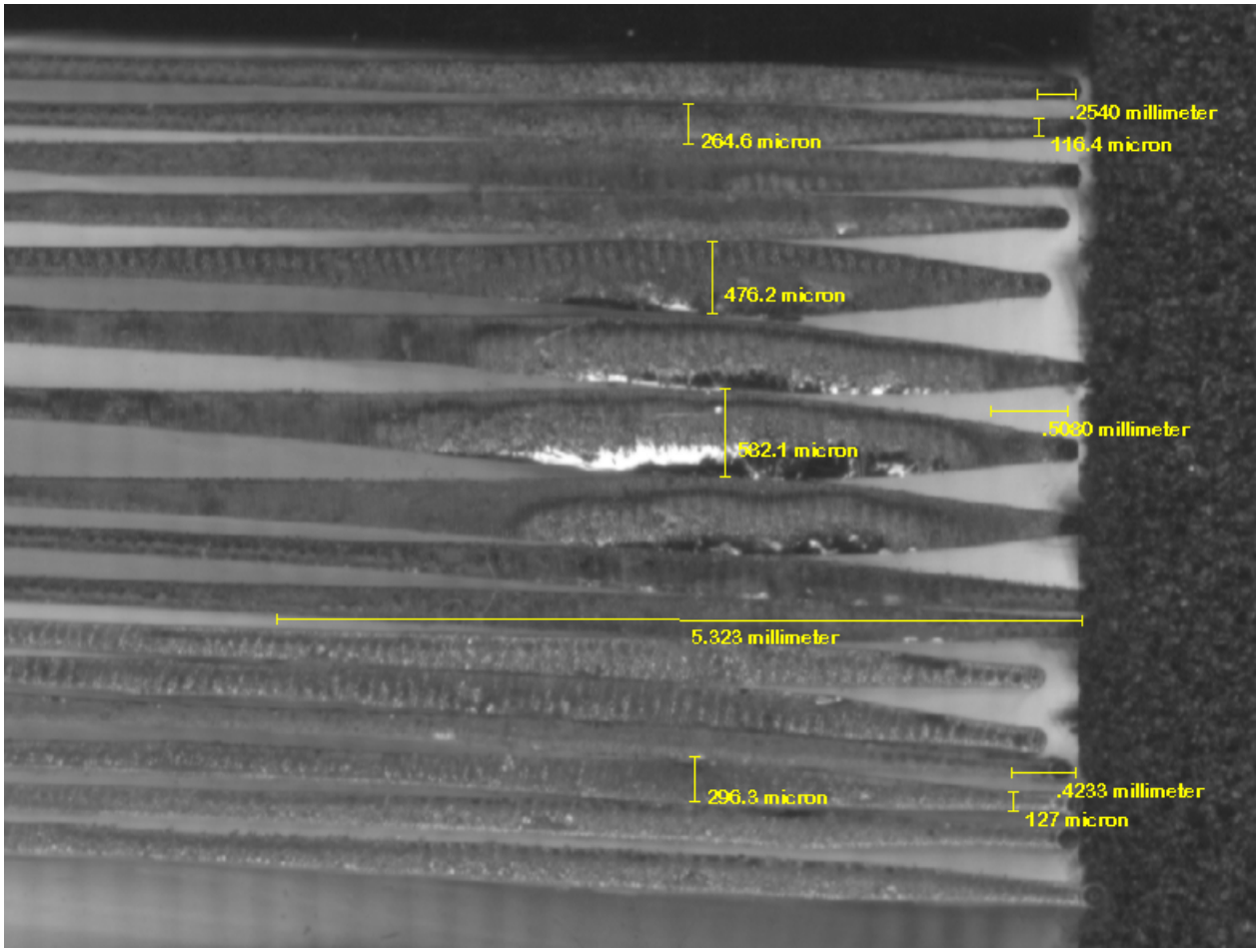

Figure 26. Thickness Variations in Wafers

Section 3- Lamination Process

This section discusses issues related to the lamination process.

Lamination Process: Top 2% of the weight distribution

This section provides an overview of modifications to the lamination process required to accommodate cells in the top 2% of the weight distribution.

The lamination stack consists of:

- Glass
- EVA
- Cell
- EVA
- Tedlar back skin

The process conditions for the lamination are:

- temperature, XXX C;
- pressure, XXX PSI;
- XXX min

Under these conditions, there is essentially no breakage in the cells. We attribute this primarily to a reduction on the cell thickness from our previous production value of 300 um to our current value of 190 um. The reduction in thickness results is a reduction in the stress in the cells during the deformation that is unavoidable during lamination. Additionally, the quality of the wafer separation cuts that are produced with the cut on the fly system is much better than was possible with the manual laser system used previously. These improved cuts have far few edge defects and the size of the defects that do exist are much smaller. This improvement in cut edge quality increases the applied stress a wafer can withstand prior to breaking.

Lamination Process: 99.5% Module Lamination Yields

This section documents the lamination yields for panels using the technology developed in this program. The details of the lamination process are presented in Lamination Process: Top 2% of the weight distribution, above.

The data in Table 16 shows quality assurance (QA) defect data for panels fabricated at our Devens facility for three days in December of 2008. These data are typical of the QA data since the factory start up in mid 2008. The data represent inspection data for a total of 1876 panel. Note that the total number of panels exhibiting broken cells is only 2, for an average defect rate of 0.1%, well below the goal of 0.5%.

Table 16. Representative quality assurance data for panels fabricated at Evergreen Solar's Devens manufacturing plant.

	Production Date		
Defect Category	14-Dec	16-Dec	18-Dec
Solder on Cell	9	2	2
RTV on Backskin	9	9	4
Frame Defect	3	10	2
Debris on Cell	10	10	12
Cracked Cell	1	1	0
Tabbing Defect	8	6	3
Marks on Glass	14	6	8
Cell Cosmetics	9	9	1
Bubble in EVA	1	0	1
Damage to Backskin	0	2	3
Lay Up Defect	0	5	5
Glass defect (inclusion, etc.)	0	5	0
Total Panels Produced	616	560	700
%Panels with cracked cells	0.16%	0.18%	0.00%

REPORT DOCUMENTATION PAGE

Form Approved
OMB No. 0704-0188

PLEASE DO NOT RETURN YOUR FORM TO THE ABOVE ORGANIZATION.

1. REPORT DATE *(DD-MM-YYYY)*	2. REPORT TYPE	3. DATES COVERED *(From - To)*
May 2009	Subcontract Report	24 June 2005 - 31 October 2008

4. TITLE AND SUBTITLE
Low-Cost Manufacturing of High-Efficiency, High-Reliability String Ribbon Si PV Modules: Final Subcontract Report, 24 June 2005 - 31 October 2008

5a. CONTRACT NUMBER
DE-AC36-08-GO28308

5b. GRANT NUMBER

5c. PROGRAM ELEMENT NUMBER

6. AUTHOR(S)
L. Felton

5d. PROJECT NUMBER
NREL/SR-520-45902

5e. TASK NUMBER
PVB75301

5f. WORK UNIT NUMBER

7. PERFORMING ORGANIZATION NAME(S) AND ADDRESS(ES)
Evergreen Solar, Inc.
259 Cedar Hill Street
Marlboro, Massachusetts

8. PERFORMING ORGANIZATION REPORT NUMBER
ZAX-5-33628-08

9. SPONSORING/MONITORING AGENCY NAME(S) AND ADDRESS(ES)
National Renewable Energy Laboratory
1617 Cole Blvd.
Golden, CO 80401-3393

10. SPONSOR/MONITOR'S ACRONYM(S)
NREL

11. SPONSORING/MONITORING AGENCY REPORT NUMBER
NREL/SR-520-45902

12. DISTRIBUTION AVAILABILITY STATEMENT
National Technical Information Service
U.S. Department of Commerce
5285 Port Royal Road
Springfield, VA 22161

13. SUPPLEMENTARY NOTES
NREL Technical Monitor: Richard L. Mitchell

14. ABSTRACT *(Maximum 200 Words)*
This report is presented to define the overall improvement process for 2008 in: 1) Adaptive Thermal Processing – to improve string-ribbon solar cell efficiency; 2) Cut-on-the-Fly (COTF) – to improve the cut-on-the-fly manufacturing process; and 3) Lamination – to improve process efficiency.

15. SUBJECT TERMS
PV; manufacturer; low cost; high efficiency; string ribbon; reliability; modules; silicon; adaptive thermal processing; lamination; solar cells; cut-on-the-fly manufacturing;

16. SECURITY CLASSIFICATION OF:			17. LIMITATION OF ABSTRACT	18. NUMBER OF PAGES	19a. NAME OF RESPONSIBLE PERSON
a. REPORT	b. ABSTRACT	c. THIS PAGE			
Unclassified	Unclassified	Unclassified	UL		19b. TELEPHONE NUMBER (*Include area code)*

Standard Form 298 (Rev. 8/98)
Prescribed by ANSI Std. Z39.18